

ENGINEERING PHYSICS MASTER THESIS PROJECT

LUND UNIVERSITY, FACULTY OF ENGINEERING

DEPARTMENT OF PHYSICS

GPX MEDICAL AB

In-vivo assessment of unwanted tissue heating during near infrared laser light emission

Martin Molin

Supervisors:

Associate Prof. Nina Reistad

Dr. Sara Bergsten

Dr. Martin Hansson

May 2020



LUND
UNIVERSITY

Acknowledgements

This work could not have been accomplished without the many tools and equipment loaned to the project by Tommy Holmqvist, Anders Persson Alexander Bengtsson and Cord Arnold at the Department of Physics.

Cord and Edouard Berrocal should also be mentioned both for interesting discussions and for great teaching in the Medical Optics course where I learnt most of the background theory that this work is founded on.

I am grateful for the contribution of Marius Plach for collaborating in screening out a suitable open-source Monte-Carlo simulation program. Åke Johansson provided the project with a computer setup powerful enough for these simulations as well as IT and technical support. The physiological expertise as well as the hospital tools provided by Malin Malmström was highly appreciated as well as the aid in the laboratory work by Safi Rafi-Zinedine.

A great thank is addressed to everyone that offered their time and energy by participating as healthy volunteers. Their contribution played a key role in that this project could be carried through.

My assistant supervisors Martin Hansson and Sara Bergsten at GPX Medical AB deserves a big thank for initialising the project and putting down many hours of their time inspiring and supervising me through it. Their inexhaustible fountain of constructive feedback and the trust they have showed in me throughout the project have contributed massively.

Last but definitely not least I want to send my most sincere thanks to my main supervisor, Nina Reistad for providing me with a majority of the resources used in the project as well as sharing her endless wisdom and precious time. Through skipped lunch breaks, evening meetings and even pandemics she pushed me forward when I got stuck and slowed me down when I went ahead of myself.

Abstract

In this work, potential adverse tissue heating in conjunction with near infrared (NIR) laser spectroscopy was studied. The tissue heating from laser light within the NIR optical window is currently a relatively unexplored field. Further knowledge of this heating is essential for the development of safe medical devices utilising laser spectroscopic diagnostics methods on living tissue.

Surface temperature increase from laser emission at wavelengths 761, 937 and 971 nm was measured on the forearms of 12 healthy volunteers. The temperature was measured with a heat camera as well as an infrared thermometer. By varying the size of the laser spot between 1-20 mm² and the power between 80-120 mW the dependence of both parameters were tested. The measured skin temperature increase from the laser illumination on all participants was below 6 °C. Furthermore a simulation of the stationary laser induced heating was produced by combining a Monte-Carlo simulation of photon migration with a finite element method simulation of tissue heating. The results of the simulations show a linear increase of the temperature as a function of the power and non-linear decrease as a function of the inverse squared radius of laser spot. By combining these dependencies a model for the predicted induced heating as a function of both the power and radius was produced. This model with the fitted coefficients from the simulations is meant to be used in aiding the development of non-invasive medical devices that utilise the optical window for diagnostics or monitoring.

All but one of the volunteers included in the project had light skin categorised as 1-3 on the Fitzpatrick scale. However a few measurements were conducted with the 761 nm laser on a volunteer with more pigmented skin of type 5. The results showed a much higher temperature increase than from lighter skin. Heating was also measured on mucosa on the inside of the lower lip on three volunteers. The measured surface temperature increases on mucosa was on the same order as for light skin.

Contents

1	Introduction	2
1.1	Purpose and scope	2
1.2	Report structure	3
2	Theory	3
2.1	Light-tissue interaction	3
2.2	Tissue and heating	4
2.3	Modelling photon migration	5
2.4	Heating in biological tissue	6
2.4.1	The finite element method	6
2.4.2	Boundary and initial conditions	6
3	Method	7
3.1	Simulation model design	7
3.2	Monte-Carlo simulation setup	7
3.3	Tissue heating simulation setup	8
3.4	Model derivation	9
3.5	Experiment setup	10
3.5.1	Mucosa heating	11
4	Results	13
5	Discussion	19
5.1	Spatial temperature increase	20
5.2	Model for skin surface heating	21
5.3	Method discussion	23
5.4	Ethical aspects	24
6	Conclusion	25
7	References	25
8	Appendix	28
8.1	Appendix A - Power meter calibration	28
8.2	Appendix B - Measurement protocol	31

Nomenclature

Symbols

Δ	Difference
ϵ	Surface emissivity
θ	Propagation angle
λ	Wavelength [nm]
μ_a	Absorption coefficient [m^{-1}]
μ_s	Scattering coefficient [m^{-1}]
μ'_s	Reduced scattering coefficient [m^{-1}]
ρ	Density [kg/m^3]
σ	Stefan-Boltzmann constant [$\text{W}/\text{m}^2 \cdot \text{K}$]
ϕ	Fluence rate [W/m^2]
ω	Perfusion rate [$\text{m}^3/(\text{kg} \cdot \text{s})$]
∇	Gradient
A	Effective area [mm^2]
c	Specific heat capacity [$\text{J}/(\text{kg} \cdot \text{K})$]
d_ϕ	Fluence rate distribution [$1/\text{m}^2$]
f	Volumetric fraction [%]
g	Anisotropy factor
h_c	Convective heat transfer [$\text{W}/\text{m}^2 \cdot \text{K}$]
k	Thermal conductivity [$\text{W}/(\text{m} \cdot \text{K})$]
$L(\mathbf{r}, \hat{\mathbf{s}})$	Light radiance [$\text{W}/\text{m}^2 \cdot \text{sr}$]
n	Refractive index
P	Power [mW]
$p(\hat{\mathbf{s}}, \hat{\mathbf{s}}')$	Scattering phase function
Q	Heat generation [W/m^3]
q	Heat flux [W/m^2]
R	Reflectance
r	Position
S	Oxygen saturation [%]
s	Direction
T	Temperature [$^\circ\text{C}$]
t	Time [s]

Abbreviations

CCD	Charge Coupled Device
CEM 43	Cumulative Equivalent Minutes at 43 $^\circ\text{C}$
FEM	Finite Element Method
GASMAS	Gas In Scattering Media Absorption Spectroscopy
Hb	Deoxygenated Haemoglobin
HbO ₂	Oxyhaemoglobin
IR	Infrared
LED	Light Emitting Diode
MC	Monte-Carlo
MCX	Monte Carlo eXtreme
NIR	Near-Infrared
RMSE	Root-Mean-Square Error
RTE	Radiative Transfer Equation

1 Introduction

Since the introduction of the microscope as a standard laboratory equipment over two centuries ago, optics has played a key role in the development of modern medicine [1]. The optical methods have rapidly accelerated our understanding of biological systems and pathology. Today they span over much larger fields than just magnifying cells and bacteria.

Many of these new fields depend on various types of lasers such as fluorescence photodetection of cancer [2], photodynamic therapy for cancer treatment [3], ultra-short laser pulses for nano-surgery [4] and optical coherence tomography for identification of melanoma [5]. These techniques are not limited to analysing tissue surfaces. By selecting laser wavelengths that are not as strongly absorbed, information from deeper within the tissue can also be extracted [6].

A well-established example of such a technique that can non-invasively and continuously monitor the health of patients is the pulse oximetry [7]. In this technique two lasers at wavelengths that are absorbed differently for oxyhaemoglobin and deoxyhaemoglobin are used and their relative absorbance measured. The relative absorbance of the wavelengths can in turn be linked to the level of oxygen saturation in the blood.

A more recent spectroscopic method developed at the Division of Atomic Physics at Lund University is called gas in scattering media absorption spectroscopy (GAS-MAS) [8]. This method utilises tunable diode laser absorption spectroscopy that is already commercially used today for example in quality assurance for packaging industry. However this technology has also shown high potential in medical applications.

The lungs are among the last organs that fully develop in infants before birth. Premature babies are therefore often born with underdeveloped lungs that risk developing various disorders [9]. A serious example of such a lung disorder is respiratory distress syndrome. It affects almost all preterm infants that are born before week 28 and can lead to chronic lung dysfunction or even death [10]. GAS-MAS has been tested for monitoring of lung function in infants with the hope of developing a reliable, continuous and non-invasive method that can pick up early signs of lung dysfunction [11]. Today the lungs of early preterm infants are monitored with repeated and potentially harmful X-ray imaging. This further reinforces the need for a new and safer monitoring technique.

The current development of a commercial product from the early research of GASMAS in medical applications is patented and run by GPX Medical AB. The company is a medical device start-up, spin-off company from the Division of Atomic Physics at Lund University. Their

method in development involves two alternating lasers in the near infrared (NIR) optical region that are scanned over known absorption peaks of water vapour and oxygen. The lasers used in the application are run at powers between 10 and 100 mW, resulting in potential heating of the illuminated tissue. Even though early testing suggests very low temperature increases there is a lack of studies focusing on tissue heating from NIR lasers with wavelengths in the tissue optical window region, in this work defined as 700-1100 nm.

There are a few previous works dealing with this topic. In an article by Bozkurt and Onaral the temperature increase from tissue absorption of two light emitting diodes (LEDs) at 730 and 830 nm with an irradiation of 37.5 mW/cm² was measured to be low, about 0.5 °C [12]. Instead the major risk of thermal damages in their study was the heat induced from the losses in the semiconductor junction of the LED that was in contact with the tissue surface. In another study by Pålsson et al. the temperature increase on light skin illuminated with an intensity of 100 mW/cm² was measured to an average of 2.2 °C from a laser at 633 nm. More pigmented skin yielded temperature increases of about 4 °C with the same setup [13]. In a third work by Ito et al. the temperature increase on both a living human forearm and excised chicken breast, illuminated with a 1 mm diameter fibre at 789 nm was measured. Their results show a linear dependence between the temperature increase and the power of the laser [14]. Furthermore the temperature increase 0.5 mm deep down in the skin of the human forearm was measured to 0.10 °C/mW but the authors state that this value is probably overestimated by about a factor 3.

In order to assess the tissue heating from NIR laser light at the specified power levels the first goal of this project was experimentally measuring this heating. The second goal of the project was then producing a model for predicting the laser induced heating from these lasers. Experiments were performed on healthy volunteers and the heating was measured with a heat camera and an infrared (IR) thermometer. Results are compared to photon migration simulations performed in a Monte-Carlo (MC) model that is combined with a finite element method (FEM) model of biological tissue heating. From the theory and the results a model of the predicted heating is derived, tested and discussed.

1.1 Purpose and scope

The key issue addressed in this work is how much biological tissue heat up while illuminated by NIR laser in the range between 700 and 1100 nm at power levels between 10 and 100 mW. This is a very broad and open ended issue which requires to be scoped down into something that could be quantified. Therefore a small number of wavelengths within this spectral range was selected for

the project. The power levels and spot sizes used was based on finding a region where the resulting heating was high enough to actually measure but small enough to not risk damaging any of the living tissue illuminated. In the time domain the stationary temperature was prioritised as the contemplated medical applications primarily uses continuous monitoring techniques. As optical and thermal properties vary between different types of tissues the core of the experiments was performed at the same type of tissue, more specifically the lateral forearm as it is easy to access and far from any extra sensitive body parts such as the eyes. The melanin concentration in the skin was also assumed to have a major influence of the results. The core of the project hence revolved around volunteers with skin of Fitzpatrick type 1 - 3.

1.2 Report structure

The relevant theory required for understanding light propagation in tissue, as well as the simulations and thermal interactions of light are presented in chapter 2. The simulation programs, selected parameter values and the experimental setup is then presented in chapter 3, Method. In this chapter a model for predicting laser-induced tissue heating is also derived. The results from both the simulations and the experimental study on healthy volunteers are presented in chapter 4. In chapter 5 the discussion of the results and methods as well as the outcomes of the project are presented together with recommendations for future studies within the field. The conclusions of the work are shortly summarised in chapter 6.

2 Theory

A large number of studies of light and its many medical applications are available in the literature. The basic theory that the work in this report is based on is presented in this part. The content is in principal summarised from the book *Optical-Thermal Response of Laser-Irradiated Tissue* [15]. Page numbers are provided and content that is added from additional sources is referenced accordingly.

2.1 Light-tissue interaction

When free photons meets the surface of a biological material the photon can either be reflected at the tissue surface or enter the tissue.

Surface reflection is depending on the refractive indices in the intersection between two media and is described by Fresnel's equations. For light normally incident on a tissue the surface reflectance, R_s is

$$R_s = \left(\frac{n_2 - n_1}{n_2 + n_1} \right)^2, \quad (1)$$

where n_1 is the refractive index of the ambient medium and n_2 is the refractive index of the tissue (p. 16).

If the photon enters the tissue it will be scattered until it either gets absorbed by some molecule in the tissue or scatters out of the tissue again. The probability for each type of interaction is depending on both the type of tissue and the wavelength (λ) of the light. If the photon is scattered through the tissue and exits on the other side it is transmitted and if it scatters around and eventually exits at the same side it entered it is diffusely reflected. An illustration of photon propagation in a thin tissue sample is illustrated in Figure 1 (p. 27-28).

The probability of absorption of a photon propagating an infinitesimal distance ds in a media is $\mu_a ds$. The corresponding probability for scattering is $\mu_s ds$. This yields the absorption and scattering coefficients, μ_a and μ_s , that describes the probability of each respectively event per unit path length. Consequently the mean free path length for an absorption or scattering event is $1/\mu_a$ or $1/\mu_s$ (p. 31).

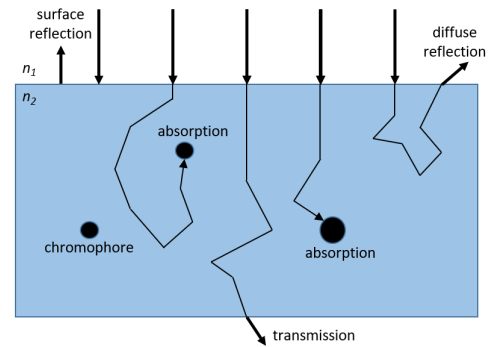


Figure 1: Illustration of photon migration in a thin tissue sample. Photons are either transmitted through the sample, reflected at the surface, diffusely reflected or absorbed by some chromophore.

The wavelength of the light is inversely proportional to the energy of each photon. Molecules absorb photons whose energies correspond to the discrete energy between their ground state and an excited state. The excited states can be either electronic, vibrational or rotational. Each electronic state has a number of vibrational states that in turn have a number of rotational states [16]. For larger molecules with more degrees of freedom the discrete energy levels starts overlapping forming a spectra of absorption probabilities. Any molecule that have the ability to absorb photons is called a chromophore. The most important chromophores in our bodies for absorbing visible light are melanin and blood. With increased wavelength the absorption for these constituents decreases while the absorption for other common constituents in the body increases. In the IR the main chromophores in human tissue are instead liquid water and fatty tissues (p. 44).

In the border between the visible and the NIR there is a wavelength range where these chromophores does not absorb as effectively. This is the so-called tissue optical window and the reduced absorption means that photons can migrate longer distances without being absorbed by the tissue. The absorption spectra for the principal chromophores in this range are presented in Figure 2.

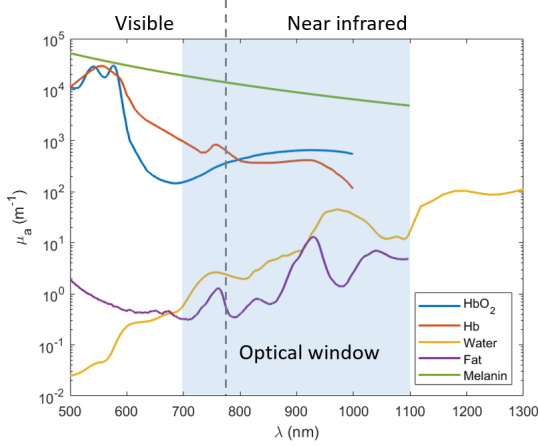


Figure 2: Absorption spectra for the main chromophores of human tissue within the tissue optical window [17, 18]. HbO₂ denotes oxygenated blood and Hb deoxygenated blood. The absorption spectra for blood is under the assumption of 150 g haemoglobin per liter of blood.

Photon migration within a highly scattering (turbid) media is a complex process. The direction a photon is launched after a scattering event within tissue is not completely random but rather heavily anisotropic. The magnitude of this anisotropy is dictated by the anisotropy factor (g) which represents the expectation value of the cosine of the scattering angle (θ). The mathematical definition for g is

$$g = \frac{\int_{4\pi} p(\hat{s}, \hat{s}') (\hat{s} \cdot \hat{s}') d\omega}{\int_{4\pi} p(\hat{s}, \hat{s}') d\omega} = \langle \cos(\theta) \rangle, \quad (2)$$

where $p(\hat{s}, \hat{s}')$ is the probability density function from the direction \hat{s}' to the direction \hat{s} and $d\omega$ is an infinitesimal interval in the solid angle between the directions (p. 46-50). $p(\hat{s} \cdot \hat{s}')$ is also known as the scattering phase function. Scattering on particles significantly smaller than the wavelength of the light, Rayleigh scattering, is isotropic while scattering on particles significantly larger, Mie scattering, is heavily directed forward. Tissue contains particles within both these categories and anything in between. The particles are also often in contact with other particles. These diverse properties of tissues makes it very hard to produce a mathematically correct version of the scattering phase function. A very commonly used approximation is the Henyey-Greenstein phase function. It originates from astronomy but has proven experimentally

to be a good approximation for tissue scattering while also being convenient to work with (p. 50-51)

$$p(\hat{s}, \hat{s}') = \frac{1}{4\pi} \left[(1-g^2) / (1-2g \cos(\theta) + g^2)^{3/2} \right]. \quad (3)$$

For tissues and light within the optical window g is between 1 and 0.7. A scattering event in an isotropic medium would yield a new direction of the photon that is completely random. For a medium with a high anisotropy this is not true. Even after one or two scattering events, most photons will still propagate in roughly the same direction. Hence, when measuring the scattering coefficient of a biological tissue the measurement will yield a lower value than the true scattering coefficient. This is called the reduced scattering coefficient (μ'_s). The correlation between the reduced and true scattering coefficient is depending on the anisotropy factor [19]

$$\mu'_s = \mu_s(1 - g). \quad (4)$$

2.2 Tissue and heating

Human skin consists of many different layers of tissue with different characteristics. A common way of categorising these layers are dividing them into three sublayers [19–21]. The outmost layer is the 20 - 100 μm thin epidermis. This layer is characterised by being the only tissue containing melanin [20, 22, 23]. As seen in Figure 2 melanin is highly absorbing within the visible and NIR. The dermis extends under the epidermis. This skin layer is about 1 - 1.5 mm thick and contain mostly blood and water. Deepest of the skin layers is the subcutaneous tissue or hypodermis. This layer is primarily characterised by its high fat content [19].

Categorisation of skin tones are often done according to the Fitzpatrick skin type scale [24]. This scale goes from 1 to 6 and in short based on the likelihood of sun burns from "always burns" to "never burns". This property is closely related to the skin pigmentation and consequently the skin tone. This rough scale for skin pigmentation is suitable for studies where melanin is expected to be a contributing factor but no strict dermatological classification can be performed. In an ex-vivo study by Simpson et al. the absorption coefficient of darker skin was determined to be much higher than for lighter skin in the visible and NIR [25].

Another type of tissue surface that can be analysed with laser based diagnostics methods is mucosa. The main difference in chromophorical composition between skin and mucosa is that the mucosa is characterised by a very high water content and does not contain any melanin [26]. There are studies on laser induced thermal treatments on

mucosa [27] but very few studies of low unwanted temperature increases from laser based diagnostic methods within the tissue optical window.

Tissue is sensitive to heating. The rate of thermal tissue damage is defined as the fraction of surviving cells per time unit under some fixed temperature. This rate is normally measured in cumulative equivalent minutes at 43 °C (CEM 43) [28]. The temperature of 43 °C is used because studies show that cell death is exponentially accelerated at about this point. A CEM 43 of about 30 - 60 min are normally used for thresholds in a successful cancer treatment (p. 539). A studie by Rhoon et al. concluded that no thermal damage occurs to any tissue below 39 °C [29].

2.3 Modelling photon migration

The ideal way of modeling photon migration in a turbid media is by using the Radiative Transfer Equation (RTE). It describes the gradient of the radiance $L(\mathbf{r}, \hat{\mathbf{s}})$ at position \mathbf{r} in the direction $\hat{\mathbf{s}}$ (p. 47)

$$\frac{dL(\mathbf{r}, \hat{\mathbf{s}})}{ds} = -\mu_a L(\mathbf{r}, \hat{\mathbf{s}}) - \mu_s L(\mathbf{r}, \hat{\mathbf{s}}) + \int_{4\pi} p(\hat{\mathbf{s}}, \hat{\mathbf{s}}') L(\mathbf{s}, \hat{\mathbf{s}}') d\omega' + S(\mathbf{r}, \hat{\mathbf{s}}). \quad (5)$$

The terms represents respectively the losses of radiant power due to absorption and scattering and the gain due to light being scattered from any direction $\hat{\mathbf{s}}'$ to the direction $\hat{\mathbf{s}}$. S is a source term where optical power is generated.

The RTE is too impractical and computationally heavy to be used directly, however an approximate solution can be found by doing some simplifications. The simplest useful approximation to the RTE is diffusion theory for light transport. This method is both fast and convenient but it is not valid close to boundaries and light-sources. The diffusion approximation also requires the medium to be heavily scattering dominated (p. 155-158).

Another approach is using Monte-Carlo (MC) simulations. The idea of a MC model is simulating the propagation of single photons, or photon behaving energy packets, one at a time. By launching a very large number of these packets an approximate solution that converges towards the true solution to the RTE can be found. There are no limiting conditions that has to be fulfilled for a MC solution to be valid making it a very versatile tool (p. 109-111). As the photons are simulated independent from each other the recent years development of parallel computing within graphical processing units have drastically improved the simulation speed resulting in that MC simulations are currently the most powerful approach for modelling advanced photon migration within turbid media [30]. A simplified flowchart of one of the first widely

used MC simulation programs called MCML is presented in Figure 3 [31].

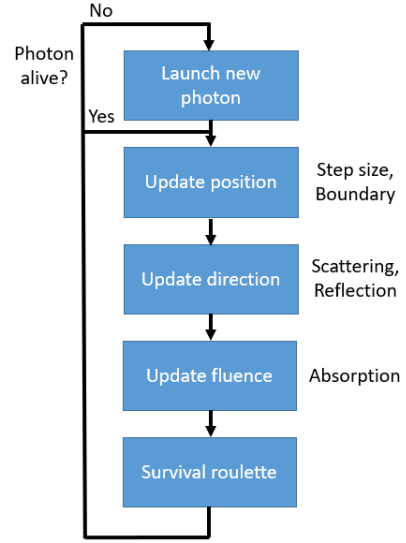


Figure 3: Simplified Flowchart for a MC simulation of photon migration. A new photon packet is first launched from the light source. In the next step the step size of the packet is randomly generated. The packet is then potentially scattered or reflected based on if it hit a boundary in the previous step. Absorption is modelled by the packet losing some of its energy in each step. The process goes on until the photon packet is terminated and a new one is launched. The packet is terminated either when leaving the medium or when losing a roulette based on its remaining energy [31].

The raw output of a MC simulation is the fluence rate (ϕ). The fluence rate is the flow of light energy per unit area at a given location in the medium.

The input parameters in most MC simulation programs for photon migration are defined for each type of media that is included in the geometry. These are the refractive index (n) the anisotropy factor (g) and the absorption and scattering coefficients (μ_a and μ_s). The absorption and scattering coefficients are crucial for modeling light propagation but different studies yields highly varying values for them, even in similar tissues [21, 32, 33]. One method for extracting generic absorption coefficient for any tissue, proposed by Jacques, is by using the volume fractions of each influential tissue chromophore [17]. These fractions are easier to either acquire or assume and they are then multiplied with its corresponding absorption spectra of concentrated matter. By summing up the contribution of each fraction the aggregated absorption spectra for an entire tissue can be extracted as

$$\mu_a = \sum_i f_i \mu_{a,i}, \quad (6)$$

where μ_a is the aggregated absorption coefficient for the

tissue, f_i is the volume fraction of constituent i and $\mu_{a,i}$ is the absorption for concentrated matter of constituent i .

A model for extracting the reduced scattering coefficient, μ'_s , for different types of tissues is also proposed in the same paper

$$\mu'_s = a \left(\frac{500 \text{ nm}}{\lambda} \right)^b, \quad (7)$$

where λ is the wavelength [17]. The model is made dimensionless by normalisation by the reference wavelength of 500 nm. The factor a is the reduced scattering coefficient for the specific tissue at 500 nm while the wavelength dependence is categorised by the scattering power b .

2.4 Heating in biological tissue

There are many approaches of modelling heating within living tissue. One popular model was developed by Pennes in 1948. This model is mathematically simple and has proven to be especially effective for modelling blood flow effects in the skin

$$\rho c \frac{\partial T}{\partial t} = \nabla \cdot (k \nabla T) + Q_{bio} + Q, \quad (8)$$

where ρ is the density, c is the specific heat capacity, T is the temperature, k is the thermal conductivity, ∇T is the gradient of T and Q is an external influence on the energy balance (p. 386-387).

The term Q_{bio} is the biological addition to the general energy conservation equation for living biological tissue. The term models temperature changes due to blood flow and metabolic heat generation

$$Q_{bio} = \omega_b \rho_b c_b (T_b - T) + Q_{met}, \quad (9)$$

where ω_b is the blood perfusion rate, ρ_b is the density of blood, c_b is the specific heat capacity of blood, T_b is the arterial blood temperature and Q_{met} is the metabolic heat generation in the tissue.

The laser induced heat is introduced in the term Q from equation (8). As a first thought one could imagine that the laser illumination is some sort of boundary term. However the absorption of the photons actually happen inside the tissue. That is where the MC simulation come into the picture. The energy induced from the laser illumination in an infinitesimal volume at a specific position in the tissue is depending on the product of fluence rate (ϕ) and the absorption coefficient (μ_a) at that position.

$$Q = \mu_a \phi = \mu_a d_\phi P. \quad (10)$$

Equation (10) presents the volumetric heat production (p. 37). The equation might require a second thought in order to make sense. The absorption coefficient is interpreted as the probability of absorption per infinitesimal path length. Multiplying the absorption coefficient with the flow of energy through a infinitesimal area hence yields the absorbed energy in the infinitesimal volume spanned by the area and path length.

As MC simulated photons are independent of each other the laser induced energy from a continuous laser source can be treated as a steady state energy flow, independent on any thermal flows within the media. The independence between the photons also yield a linear dependence between the fluence rate and the number of photons in the media. Consequently the fluence rate (ϕ) is linearly dependent on the power (P) (p. 115). Hence, the fluence rate can be rewritten as $d_\phi P$ where $\mu_a d_\phi$ is interpreted as the steady state absorption distribution of the power P .

2.4.1 The finite element method

The differential equations for energy conservation above can only be solved analytically for very simple geometries and even then the process is time consuming and ineffective. By using numerical integration an approximate solution to the differential equations can be found in a much more time effective manner. These solutions for more advanced geometries can also be found by dividing the geometry into a mesh of small and simple geometries [34]. Each of these geometries are then regarded as an element of the problem. This is the basis of the finite element method (FEM).

2.4.2 Boundary and initial conditions

A FEM mesh is not infinitely large and for that reason the behaviour of the edges of the model must be defined. This is done by assigning specific properties to the surface nodes of the most shallow elements in the mesh. These are called boundary conditions and are described in more detail in this section.

A type of boundary condition that are common in heat transfer is based on the heat flux, the gradient of the temperature (∇T). Far away from any external heat sources assuming that the edge will not affect the solution a homogeneous solution is suitable. This corresponds to perfect thermal insulation. Especially for systems with thermal and geometrical symmetry this is a suitable condition (p. 384)

$$k \nabla T = 0. \quad (11)$$

Modelling parts that are in thermal contact with its environment results in more interesting boundary conditions.

For skin affected by ambient air the two governing phenomena are convective heat flux and thermal radiation. The convective heat flux is due to relative motion between the ambient air and the tissue. The equation for the convective heat flux is

$$q = h_c(T_{amb} - T), \quad (12)$$

where h_c is the convective heat transfer coefficient and T_{amb} is the ambient temperature (p. 361-362).

All objects emits thermal radiation. An object with a higher temperature than the ambient temperature will lose energy according to

$$q = \epsilon\sigma(T_{amb}^4 - T^4), \quad (13)$$

where ϵ is the surface emissivity for skin and σ is the Stefan-Boltzmann constant.

Humans also have the ability to cool down their body temperatures by evaporating water at the skin surface, a process known as sweating. Mathematically modelling energy flow conducted by sweating is complicated and involves a number of environmentally depending terms. However in the case of low temperature increases induced by local laser illumination, sweating is not a major factor [35].

3 Method

Both simulations and experiments were performed for analysing the different aspects of laser induced tissue heating. For the simulation, the programs, the model setup and the process of extracting good parameter values are presented. For the experimental study, the laboratory setup and the participating healthy volunteers are presented in this section.

3.1 Simulation model design

A cylindrical tissue model with the radius 40 mm was created for mimicking the forearm geometry. The length of the cylinder was set to 80 mm. The hardware available limited the simulation from using of a mesh fine enough for resolving the ultra thin epidermis layer. Instead a 1 mm thick combined skin layer of the dermis and epidermis was created. The subcutaneous fat layer was set to 2 mm thick and the remaining volume consisted of muscle tissue. As the experiments were performed on the muscular ventral side of the forearm as seen in Figure 10 the bone was assumed to be too deep inside the tissue to have any significant impact of the simulation. The ambient medium was air. The origo was placed in the center of the cylinder and the laser was illuminated along the negative z -axis. The length of the cylinder was set so that

the circular sides were too far from the laser illuminated spot to influence the solution in any significant way. The model geometry is shown in Figure 4.

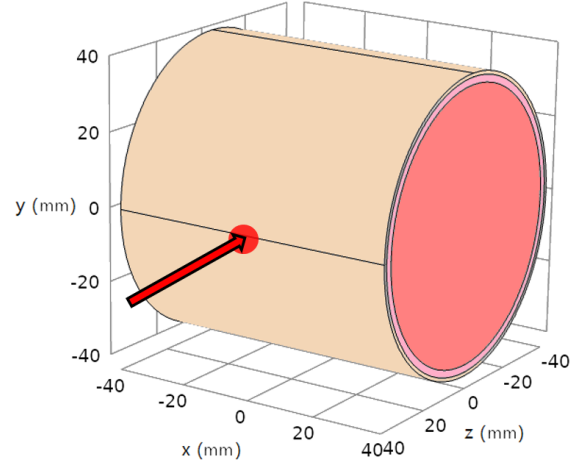


Figure 4: Cylinder model of the laser illuminated forearm that was used in the simulations. The radius of the cylinder was 40 mm and its center was located in origo. The length of the cylinder was 80 mm and followed the x -axis. The laser illumination was incident along the negative z -axis. The model consisted of three tissue layers where the outmost skin layer was 1 mm thick, the underlying subcutaneous fat layer was 2 mm thick and the rest consisted of muscle tissue. The layers are coloured beige, pink and red respectively for a better illustration.

3.2 Monte-Carlo simulation setup

The MC simulation for photon migration was performed in an open source program available for downloading online called Monte-Carlo eXtreme (MCX) [30]. Grids in MCX are based on cubic voxels and the program features the Henyey-Greensteins scattering phase function (3). The model in Figure 4 was created in a uniform grid of 160^3 cubic voxels, each with the side 0.5 mm. The voxels excluded from the geometry were ambient air ($n = 1$, $\mu_s = 0$, $\mu_a = 0$).

The light source was set outside the figure directed in the negative z -direction, centered in $x = y = 0$. The beam profile was set to be a uniform disk (circular flat-top) in order to effectively mimic the properties of the effective area of a laser spot [36, 37]. The radius of this disc was varied between 0.5 and 5 mm in order to obtain different effective areas.

The refractive index (n) and anisotropy factor (g) for the tissue layers are presented in Table 1.

The absorption coefficients were acquired by using the model in (6). The absorption spectra for the concentrated matter of the main chromophores in human tissue at the examined wavelengths are extracted from the data in Fig-

Table 1: Refractive index and anisotropy factor for the MC simulations of photon migration in the tissue layers of a human forearm.

Tissue layer	n	g	Source
Skin	1.40	0.85	[19, 20]
Subcut. fat	1.45	0.80	[19, 20]
Muscle	1.40	0.90	[17]

ure 2 and presented in Table 2. The corresponding volume fraction for each constituent is presented in Table 3.

Table 2: The absorption coefficients for concentrated matter of the main chromophores of human tissue for the specific wavelengths [17, 18].

Constituent	Absorption, μ_a (m^{-1})		
λ (nm)	761	937	971
HbO ₂	317	651	621
Hb	821	383	226
Water	2.63	23.2	45.2
Fat	1.29	10.7	1.51
Melanin	14.7e3	7.89e3	7.09e3

Table 3: The volume fractions of the main chromophores in living human tissue in the NIR. The term f_b corresponds to the fraction of blood, f_w the fraction of water, f_f the fraction of fat and f_{mel} the fraction of melanin which is only found in the epidermis. The term S is the average oxygen saturation of the blood as oxygenated and deoxygenated blood posses different optical properties. The melanin content is based on 0.87% in a 60 μm thick epidermis evenly distributed over a 1 mm thick skin layer. The fractions are given in volume %. [17].

Tissue layer	f_b	S	f_w	f_f	f_{mel}
Skin	0.34	64	55	28	0.052
Subcut. fat	0.76	64	15	55	0
Muscle	1.60	64	70	0	0

The reduced scattering coefficients for the different tissue layers are extracted by using the model in equation (7). In order to use this model the coefficients a and b must be selected. These are presented in Table 4. Before using the coefficients as parameters in the MC simulation the normal scattering coefficients, μ_s , must be extracted from the reduced form, μ'_s , by using equation (4). The final scattering and absorption coefficients used in the MC simulation are presented in Table 5.

An example of the output fluence rate (ϕ) in the xz -plane from the MC simulation is presented in Figure 5.

In order to make the tissue heating simulation independent of any optical parameters the volumetric heat production (Q) from equation (10) was extracted directly from the MC simulation. This was done by multiplying the fluence rate (ϕ) and the absorption coefficient (μ_a) in each voxel of the grid. By default the total power in the

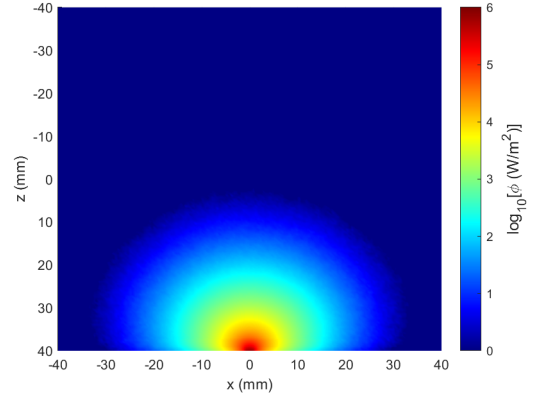


Figure 5: The \log_{10} fluence rate (ϕ) in the xz -plane of the forearm. The forearm is illuminated by the 937 nm laser with a spot size of 3.1 mm^2 and a power of 1 W. This is an example output from the MC simulation.

MC simulation output was normalised to 1 W. Before usage in the tissue heating simulation the output from the MC simulation had to first be multiplied with the true power (eg. 0.1 for 100 mW). This can be done as the steady state absorption distribution ($\mu_a d_\phi$) is independent of the the power (P).

Table 4: Factors for extracting the reduced scattering coefficients [17].

Tissue layer	a (m^{-1})	b
Skin	3680	1.160
Subcut. fat	1470	0.672
Muscle	1510	1.290

3.3 Tissue heating simulation setup

The program Comsol Multiphysics was used for the FEM model of tissue heating. The model geometry is visualised in Figure 4. The FEM mesh of the geometry consisted of about 107000 non-uniform tetrahedral elements. The element quality was refined down to triangles with a side length of 0.1 mm along a 10 mm line on the optical axis incident on the tissue surface. The biological heating differential equation that is governing the simulation is presented in equation (9). On the circular sides of the model, defined by $x = \pm 40$ mm, thermal insulation was set as these sides were assumed to be too far from the laser illumination to significantly affect the result.

The tissue surface defined by $y^2 + z^2 = 40$ mm is where the simulated tissue was in thermal contact with its environment. There both convective heat flow (12) and thermal radiation (13) was set as boundary terms. Within the low temperature increases of this project water evaporation by sweating was omitted. The laser induced energy is emerging inside the tissue as a function of the MC sim-

Table 5: Optical coefficients for the tissue layers used in the MC simulation.

Tissue layer	Absorption, μ_a (m^{-1})			Scattering, μ_s (m^{-1})		
λ (nm)	761	937	971	761	937	971
Skin	11.2	21.8	30.6	13500	10100	9570
Subcut. fat	4.89	13.6	11.2	5550	4830	4710
Muscle	9.81	25.1	39.3	8820	6750	6450

ulated fluency rate and is described in equation (10). The simulated fluence rate from MCX was transcribed to a .txt file and then imported into Comsol.

As the project was focused on assessing the stationary temperature at thermal equilibrium, an exact initial temperature was not crucial for the result. A reasonable value however lead to faster convergence. The initial temperature was therefore set to the arterial blood temperature (T_b) in the whole geometry. However a small number of time-dependent simulations was performed for comparison with the experimental data. For these simulations the stationary temperature without any laser illumination was first simulated and then used as initial temperature in the time-dependent simulations.

A large number of parameters were used in the FEM simulation. Comsol contains a library of many standard material parameters. The parameters used from this library are presented in Table 6. However, most parameters used were from previous studies. These are all presented in Table 7.

An example of the output temperature (T) in the xz -plane from the tissue heating simulation is presented in Figure 6.

Table 6: Standard material properties in Comsol for skin (epidermis and dermis), fat (hypodermis) and muscle. k is the thermal conductivity, ρ is the density and c is the specific heat capacity. The same parameter values are found in the IT'IS database [38].

Symbol	Skin	Subcut. fat	Muscle	Unit
k	0.37	0.21	0.49	W/(m·K)
ρ	1110	911	1090	kg/m ³
c	3390	2350	3420	J/(kg·K)

3.4 Model derivation

What are the dependencies between the temperature increase, the power and the laser spot size? By studying a highly simplified case, a model for these two dependencies are derived. In Figure 5 an example of the fluence rate from the MC simulation is presented. The shape of the distribution can roughly be described as a hemisphere with a radius (r_s) where the base is the laser illuminated skin surface. In order to simplify the distribution even further we assume a homogeneous media and that the flu-

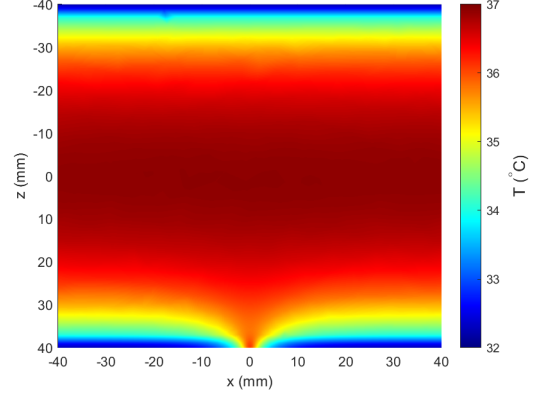


Figure 6: The temperature (T) in the xz -plane of the forearm. The forearm is illuminated by the 937 nm laser with a spot size of 3.1 mm² and a power of 100 mW. The temperature increase is distinct close to the laser illuminated spot but quickly fades out in the remaining geometry. The core temperature of the arm is about 37 °C and temperature of the undisturbed skin surface is about 32 °C. This is an example output from the FEM simulation.

ence rate is uniform within the hemisphere. This hemisphere of uniform light fluence is presented in Figure 7.

In Figure 7 a laser beam with the power (P) and radius (r_l) is illuminated on the tissue surface. In this highly simplified case the thermal interactions at the skin surface, such as convection and thermal radiation, as well as the biological interactions (Q_{bio}) are all omitted. The tissue surrounding the hemisphere is unaffected by the laser illumination and is assumed to have the constant temperature (T_0). As the hemisphere gets heated by the laser light there will be two net flows of energy through the sphere. These are the energy deposited by the laser and the energy flux through the surface area due to heat diffusion

$$\begin{aligned} q_{in} &= P \\ q_{out} &= -Ak(T - T_0), \end{aligned} \quad (14)$$

where A is the surface area of the hemisphere and k is the thermal conductivity. The surface temperature (T) is assumed to be the same on both the base and surface area of the hemisphere. As the surface area for a hemisphere is $2\pi r^2$ the energy balance can be described as

Table 7: Parameters used in the FEM simulation of laser induced tissue heating. The blood perfusion parameter for skin ($\omega_{b,s}$) was used both in the skin and subcutaneous fat tissue.

Description	Symbol	Value	Unit	Source
Ambient temperature	T_{amb}	21	$^{\circ}\text{C}$	
Arterial blood temperature	T_b	37	$^{\circ}\text{C}$	
Blood density	ρ_b	1050	kg/m^3	[38]
Blood perfusion muscle	$\omega_{b,m}$	1.4e-3	1/s	[15, 39]
Blood perfusion skin	$\omega_{b,s}$	5.5e-4	1/s	[15, 39]
Blood specific heat capacity	c_b	3617	$\text{J}/(\text{kg}\cdot\text{K})$	[38]
Convective coefficient	h_c	8	$\text{W}/\text{m}^2\cdot\text{K}$	[19, 40]
Metabolic heat production	Q_{met}	1430	W/m^3	[40, 41]
Skin emissivity	ϵ	0.996	-	[42]
Stefan-Boltzmann constant	σ	5.68e-8	$\text{W}/(\text{m}^2\cdot\text{K})$	[15]

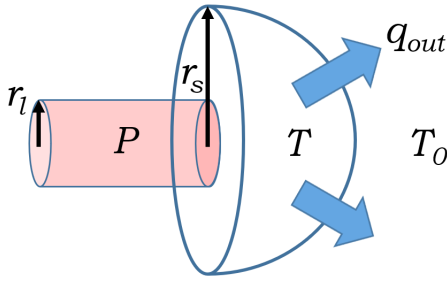


Figure 7: Homogeneous tissue hemisphere of uniform fluence. The circular base of the hemisphere with radius (r_s) is the skin surface illuminated by a laser with power (P) and radius (r_l). The deposited energy from the laser will yield a temperature increase within the hemisphere in turn resulting in flow of energy through the surface area with the temperature (T) into the surrounding tissue with the constant temperature (T_0).

$$\frac{\partial Q_s}{\partial t} = P - 2\pi r_s^2 k(T - T_0). \quad (15)$$

In the stationary case where thermal equilibrium has been reached the left hand side of (15) will be zero. The temperature increase on the surface of the hemisphere ($\Delta T = T - T_0$) can then be described as

$$\Delta T = \frac{P}{2\pi k r_s^2}. \quad (16)$$

From the expression in (16) one can expect that the temperature increase at the tissue surface (ΔT) will be linearly depending on the power (P).

How does the radius of the tissue sphere (r_s) in equation (16) correlate to the radius of the laser spot (r_l)? As tissue is highly scattering it is very unlikely that the radius of the illuminated tissue sphere would also decrease to zero if the laser illuminated spot was very small. This would also generate a temperature increase very rapidly moving towards infinity which does not seem true. As photons

migrating in a tissue are independent of each other the scattering and absorption in the tissue is independent of the geometry of the laser spot. Therefore it is reasonable to assume that there will be an offset between these two radiuses that is depending on the absorption and scattering. At a specific wavelength in a specific tissue this offset would be constant as

$$r_s = r_l + r_0, \quad (17)$$

where r_0 is the offset between the two radiuses. The surface temperature increase (ΔT) as a function of the of the laser spot (r_l) would then take the form

$$\Delta T = \frac{a \cdot P}{(r_l + r_0)^2}, \quad (18)$$

where $a = (2\pi k)^{-1}$ and r_0 are coefficients that can be fitted to the data from both simulations and experiments. P is the power and r_l is the radius of the laser spot. The equation in (18) for the surface temperature increase as a function of the power and radius of the laser spot will be tested in this work.

3.5 Experiment setup

Three unlabeled laser diodes were one at a time connected to a laser diode driver (Thorlabs LDC220C) and a thermoelectric cooling unit (Thorlabs TED200C). The thermoelectric cooling unit was set so that each laser diode remained at room temperature and the laser diode drive current could be varied in order to adjust the output power. By using a spectrometer (Qmini AFBR-S20M2VN) the output wavelengths of the diodes were measured to 761, 937 and 971 nm. Since the three diodes all had different output profiles each diode required a specific set of optics for directing the laser beam onto the tissue surface. These optical elements consisted of 2-3 lenses and a shutter and were placed on a rail aligned with the laser beam. A stage for placing the samples was put on the far end of the rail.

The laser beams was guided over the center of the sample stage and through a collector lens in the far end, focusing the laser light on the detector of laser power meter (Ophir Nova II). The detector of the power meter was a sensitive photodiode with a window of about 1 cm², hence the need for a collector lens. The power meter required calibration, both generally and for the losses in the collector lens. This was done by comparing it with a similar power meter which was more recently calibrated. The data from the power meter calibration is presented in Appendix A.

A CCD camera (Thorlabs DCU224M) was placed behind the sample stage for spot size imaging. The size and profile of the laser spot was extracted by illuminating a thin sheet of white paper with the laser at low power. The transmitted laser profile was imaged by the CCD camera. The shutter and laser power was adjusted in order to not over-expose the camera. The gain in the camera software was turned off and the gamma was set to 1 in order to not distort the representation of the laser profile. An image of a ruler located at the same spot as the paper sheet was also captured as a size reference. From the image of the transmitted laser profile the effective area of the laser profiles was extracted. The effective area is represented by the circular area of an ideal flat top laser beam whose total energy is equal to the total energy of the laser spot. For a normalised laser profile this geometrically corresponds to the circular area of a cylinder with the height one and the same volume as the imaged profile [36, 37]. The effective area is a method for spot size analysis that does not require any specific shape of the laser profile. The profiles of the laser spots from the three diodes and their corresponding effective areas are presented in Figure 9.

Surface temperatures were measured both by using a thermal camera (Flir C2) and an IR thermometer (Optris CT LT) with a close focus lens. The thermal camera was placed 15 cm in front of the sample location as close to in line with the laser beam as possible. The IR thermometer featured a very narrow and close focus, 0.6 mm in diameter at a distance of 10 mm from the lens. It was placed at the sample surface in an angle of about 45 degrees, facing the center of the laser spot at the sample surface without interfering with the laser beam. A metal coin with the diameter 19.5 mm was taped to the surface of the forearm, beside the laser illuminated spot in order to be able to extract spatial resolution from the heat camera data. A conceptual sketch of the laboratory setup is shown in Figure 8.

The correct position of the IR thermometer was found by laser heating a black plastic box whose temperature increase was many times larger than the temperature increase in the tissue. The position of the thermometer was then adjusted until reporting the same or higher temperature than the heat camera.

At $t = 0$ s the IR thermometer started measuring. At t

$= 10$ s the heat camera started measuring. At $t = 30$ s the laser was turned on. The laser was then illuminating a spot of the surface of the forearm for 3 minutes before being turned off at $t = 210$ s. After the laser was turned off the heated spot on the forearm was allowed to cool down for 3 minutes. At $t = 390$ s the heat camera measurement was turned off and at $t = 400$ s the IR thermometer measurement was turned off. The full measurement protocol is presented in Appendix B.

For each new measurement either the power or effective area of the laser spot was varied. The powers used were 80, 100 and 120 mW. The effective areas of the laser spots were not varied between specific values as the extraction of these values required some computer analysis. Instead the spots were adjusted based on some earlier spot size images. The exact values were then extracted after the measurements and ranged between 1 and 20 mm². The ranges were selected as initial trials indicated both measurable levels of heating and low enough temperatures for not potentially causing any thermal damage, for all three lasers.

The measurements were performed on the right ventral forearm of a group of 12 healthy volunteers at different genders and ages. The individuals of the group is presented in Table 8. The Fitzpatrick skin types were assumed based on the skin tone. Person 1 was illuminated by all lasers, powers and spot-sizes and thereby provided a baseline for the other measurements.

Table 8: The 12 healthy volunteers that participated in the study. M is for male and F for female. N data is the amount of measurements performed on the person. The experiments were performed in late winter on untanned volunteers with light skin. The volunteers with type 1-2 had slightly lighter skin than the rest of the group but it is not certain whether they were light enough for being classified as type 1. Three measurements were performed on person 12 with much more pigmented skin.

Person	Gender	Age	Skin type	N data
1	M	24	2	47
2	F	23	1-2	2
3	M	24	1-2	9
4	F	27	3	3
5	M	42	2	6
6	M	24	2	6
7	F	46	1-2	9
8	F	59	2	6
9	M	60	2	6
10	F	25	2	6
11	F	46	2	1
12	M	38	5	3

3.5.1 Mucosa heating

A minor pilot study on the resulting laser-induced heating on mucosa in the same range of powers and spot sizes

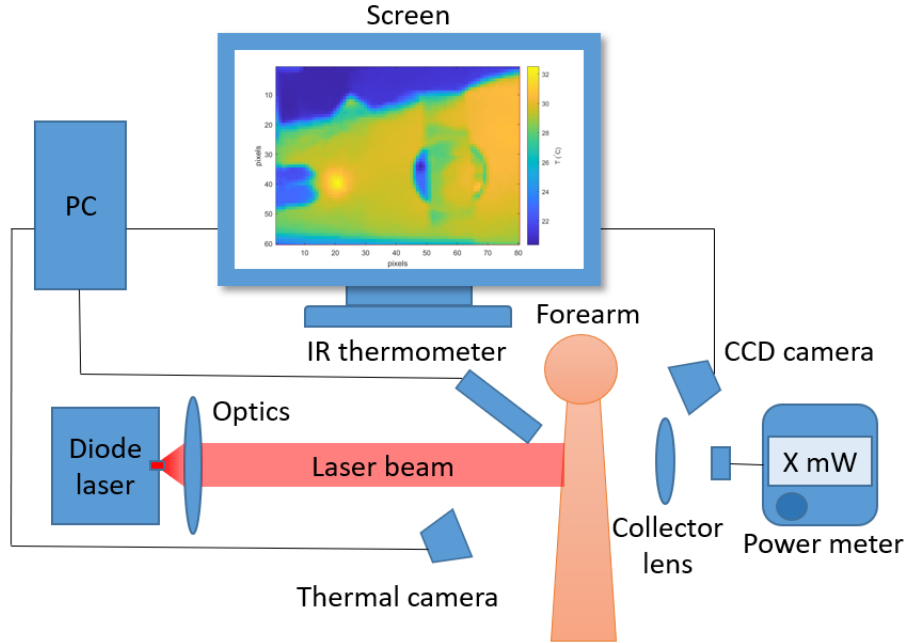


Figure 8: Conceptual sketch of the experimental setup. The diode laser is illuminating the forearm while the temperatures are measured by the thermal camera and the IR thermometer. Before each measurement the laser power is measured by the power meter and the spot profile is captured by the CCD camera in order to extract its effective area.

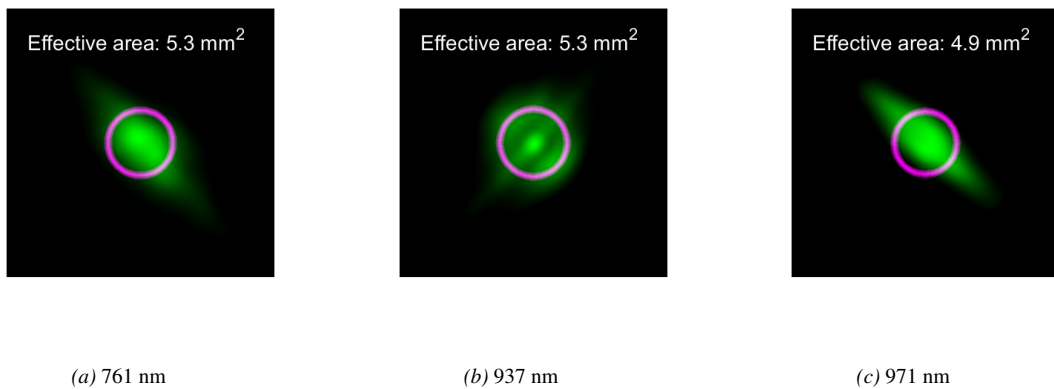


Figure 9: Laser spot profiles for the three different lasers focused down to about 5 mm² and represented by the green shape. Their corresponding effective areas are illustrated by the purple circle. Spatial dimensions were extracted by capturing an image of a ruler placed at the same spot as the sheet of illuminated paper. The elliptic shapes are because of the highly rectangular outputs of the laser diodes and the diagonal tilt is because of the orientation of the CCD camera.

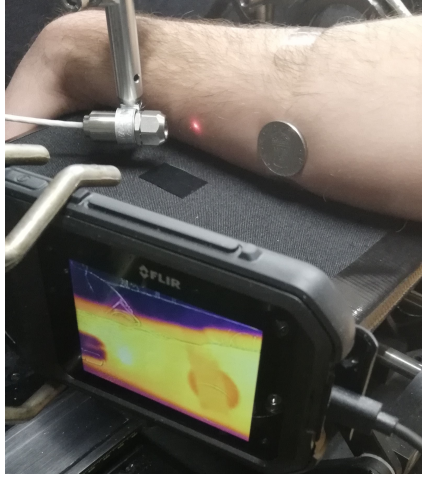


Figure 10: Forearm illuminated by the 761 nm laser. The IR thermometer is placed approximately 10 mm in an angle from the skin. The heated spot in the heat camera recording is distinguishable on the camera screen. The coin is used for extracting the spatial resolution from the heat camera recording. The skin of the forearm in the image is classified as type 2.

was performed. The same method as for the forearm measurements was used but the setup was adjusted by putting an opticians stage at the edge of the optical table. The power meter and CCD camera were made mobile by placing them in a magnetic switchable device, as their position no longer could be stationary behind the measured sample. The power meter and CCD camera were then moved in the line of the laser beam between each mucosa measurement for extracting the illuminated spot size and power. The close focus lens of the IR thermometer was also removed yielding resolution with a 22:1 field of view. The lower lip of the volunteers was folded out, revealing the mucosa that was illuminated by the laser. This is visualised in Figure 11. The three volunteers that were participating in the study on mucosa are presented in Table 9.

Table 9: The three volunteers for the study of laser induced heating of mucosa.

Person	Gender	Age	N data
1	F	46	4
2	M	34	4
3	M	29	3

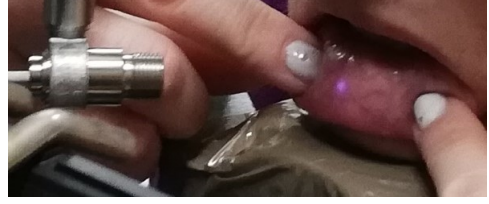


Figure 11: Mucosa illuminated with the 971 nm laser. The chin of the volunteers were placed on an opticians stage at the edge of the optical table and the lower lip was folded out revealing the mucosa inside. The NIR laser light was invisible to the eye but could effectively be captured by a standard digital camera.

4 Results

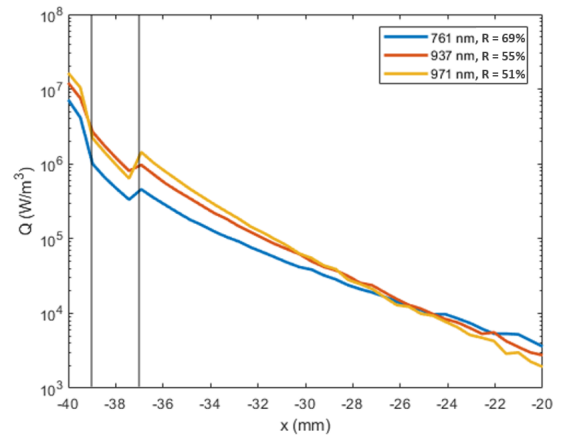
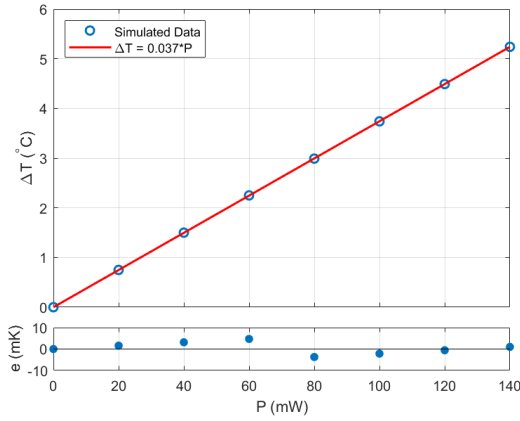


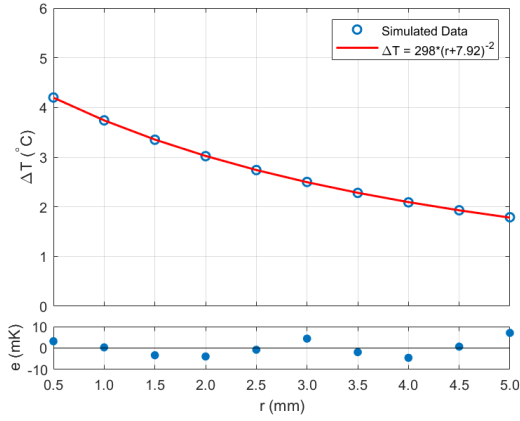
Figure 12: The volumetric heat production (Q) in the tissue along the optical axis. These simulations were run with 3.1 mm^2 circular laser spots and the total power in each MC simulation was 1 W. The notches in the initial part of the curves are because the absorption differs between the different tissue layers. The vertical grey lines denotes the edge of each tissue layer. The reflectance of each wavelength is presented in the legend.

The volumetric heat production (Q) in the tissue along the optical axis of the laser beam is presented in Figure 12. A majority of the total simulated energy was lost due to diffuse and surface reflection before it got absorbed in the tissue. The percentage of reflected photons at each wavelength are presented in the legend.

The model in (18) with coefficients fitted to the simulated data is plotted in Figure 13. As the model is derived based on the radius of the laser spot, the plots in this chapter are presented as a function of the radius ($r = \sqrt{A/\pi}$) and not the area (A).



(a) The simulated temperature increase (ΔT) through the laser power (P) of the tissue surface illuminated by the 937 nm laser with a spot radius of 1 mm. The simulated temperature increase and power features a linear correlation presented by the fitted line. The residues of the fit are plotted below.



(b) The simulated temperature increase (ΔT) of the tissue surface through the radius (r) of the laser spot illuminated by the 937 nm laser at 100 mW. The residues of the fit are plotted below.

Figure 13: The simulated laser induced temperature increase (ΔT) of the tissue surface as a function of the power (P) and radius (r) of the laser spot illuminated by the 937 nm laser. The fits are based on the model in (18).

12 simulations of the stationary temperature increase from laser illumination of a human forearm was performed per wavelength. Three different power levels and four different spot sizes were used. The temperature increase was extracted by subtracting the baseline from a simulation of the forearm temperature without any laser illumination. The coefficients, a and r_0 for the model in (18) was fitted for each data set of simulated temperature increase by using the least square method. The resulting surfaces are illustrated in Figure 14 and their coefficients are presented in Table 10.

The data from the experimental study is presented in the scatter plots of Figure 15. The semi-transparent surfaces represents the model in (18) with coefficients a and r_0 fit-

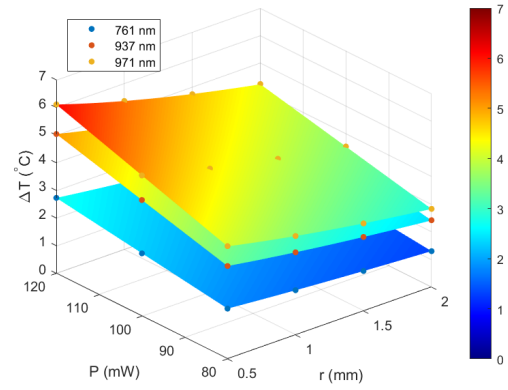


Figure 14: The simulated temperature increase (ΔT) as a function of the power (P) and radius (r) of the laser spot. The surfaces are the model in (18) plotted with the coefficients in Table 10 that are fitted to the simulated data. The 971 nm laser results in the highest laser induced heating and the 761 nm in the lowest.

Table 10: The coefficients of the model in (18) fitted to the simulated data in Figure 14. The quality of the fits are given in terms of root mean square errors (RMSE).

λ (nm)	a ($\text{K} \frac{\text{mm}^2}{\text{mW}}$)	r_0 (mm)	RMSE ($^{\circ}\text{C}$)
761	1.55	7.42	2.2e-3
937	2.93	7.85	2.2e-3
971	2.87	7.00	3.2e-3

ted for each wavelength of the experimental data. The coefficient values are given in Table 11. The mean deviation from the surfaces for each volunteer in the experimental study is presented in Table 12.

There were in total 11 measurements performed on the mucosa of the inside of the lower lip of three healthy volunteers. The measured laser induced heating is presented in Table 13

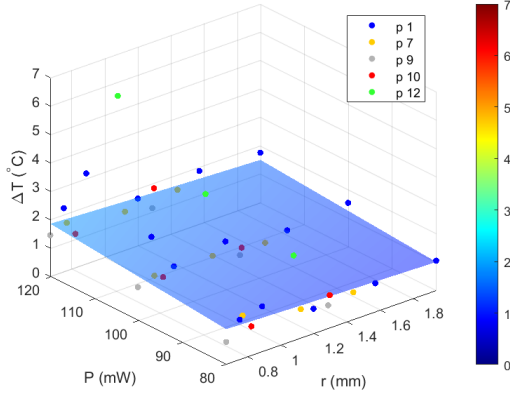
Table 11: The coefficients of the model in (18) fitted to the data from the experimental study presented in Figure 15. The RMSE for the fits are also presented.

λ (nm)	a ($\text{K} \frac{\text{mm}^2}{\text{mW}}$)	r_0 (mm)	RMSE ($^{\circ}\text{C}$)
761	2.09	10.9	0.30
937	0.111	1.53	0.28
971	2.33	7.41	0.28

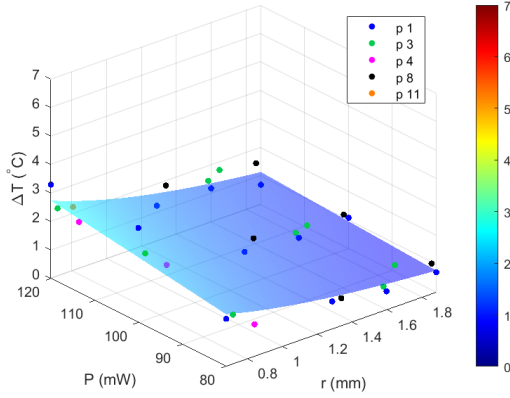
The temperature increase as a function of the intensity of the laser light for both the experiments and simulations are presented in Figure 16.

The correlation between the data from the two temperature measurement methods are presented in Figure 17.

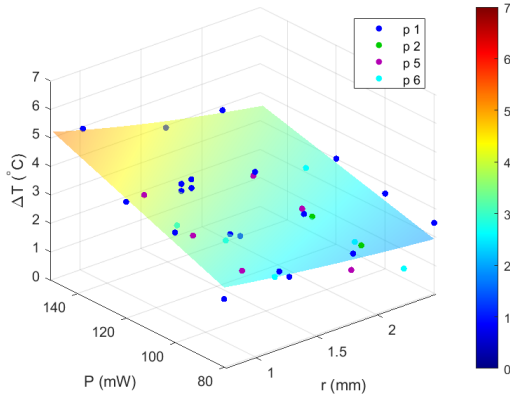
The experimental temperature increase was measured over a time of 3 min. The temperature development over time



(a) Data and model surface for the 761 nm laser.



(b) Data and model surface for the the 937 nm laser.



(c) Data and model surface for the 971 nm laser.

Figure 15: The measured temperature increase (ΔT) from the experiments as a function of the power (P) and the radius (r) of the laser spot. The semi-transparent surfaces are the model in (18) plotted with the coefficients in table 11 that are fitted to the experiment data. The colours of the dots relates to each person in Table 8.

Table 12: The mean deviation between the measured temperature increase on each of the volunteers and the model in (18) with coefficients fitted to the experiment data. Person 12 was excluded from the the fit as his level of pigmentation was a lot higher than the rest of the studied group. This person is also the only volunteer reporting a deviation larger than two RMSE from the fit. The largest deviation from the fit in the rest of the group was measured on person 4, 6 and 9 that all reported lower temperature increases than the average.

Person	λ (nm)	Deviation ($^{\circ}\text{C}$)	Deviation (%)
1	all	+0.13	+5.5
2	971	+0.23	+11
3	937	+0.12	+11
4	937	-0.50	-25
5	971	+0.14	+4.3
6	971	-0.54	-20
7	761	-0.12	-7.4
8	937	+0.17	+16
9	761	-0.41	-28
10	761	-0.17	-10
11	937	-0.18	-8.0
12	761	+2.61	+177

Table 13: The temperature increase from illumination of mucosa. The data is presented as deviation from model in (18) with coefficients fitted to the experimental data on light skin. The results vary between the participants but the deviations do not differ much from the measurements on light skin.

Person	λ (nm)	Deviation ($^{\circ}\text{C}$)	Deviation (%)
1	971	-0.38	-13
2	971	+0.42	+15
3	761	+0.42	+29

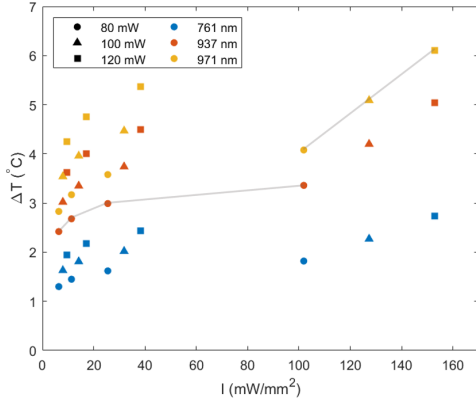
was also simulated. These are both presented in Figure 18.

The experimental and simulated results are plotted together in Figure 19. In order to plot the data on a single axis the dependence in the constant axis was subtracted from each data point as

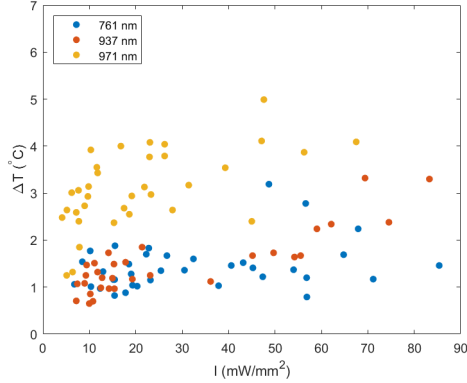
$$\Delta T(x, C) = \Delta T(x, y) - (f(x, y) - f(x, C)), \quad (19)$$

where ΔT is the experiment data, x is the dependent variable, C is the constant value of the constant axis, y is the dependent variable of the constant axis and f is the model in (18) with coefficients fitted to the experiments.

The temperature increase in the whole laser illuminated forearm was acquired in the simulations. In the left plots of Figure 20 the simulated temperatures inside the tissue along the optical axis are presented for different wavelengths, spot sizes and powers. The right plots show the temperature increase of the skin surface with the same parameters varied.



(a) The simulated temperature increase (ΔT) through the intensity of the laser light (I). Increasing the power over a constant laser spot size yields a linear temperature increase. Decreasing the laser spot size over a constant laser power instead result in a non-linearly, plateauing temperature increase. These dependencies are highlighted by the dots bound together by the grey lines. There is no linear correlation between the resulting heating and the laser intensity.



(b) The experimental temperature increase (ΔT) of the forearm through the intensity of the laser light (I). As in the simulated case, it does not seem to be any linear correlation between the illuminated intensity and the temperature increase.

Figure 16

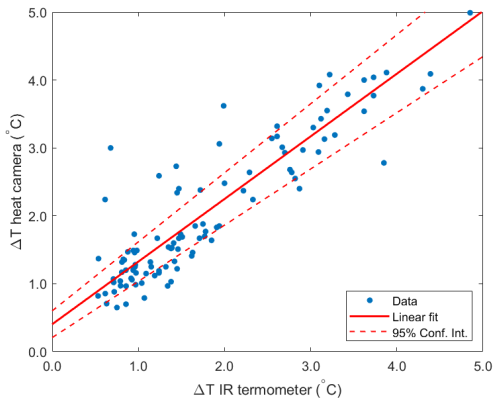
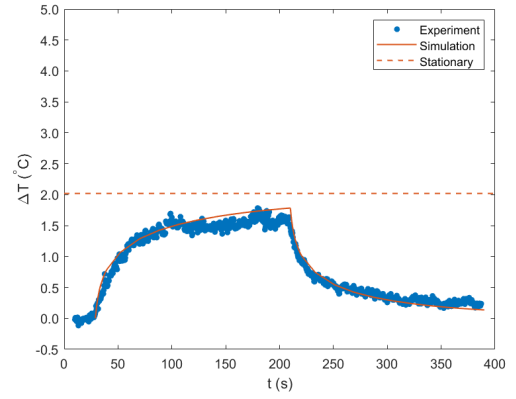
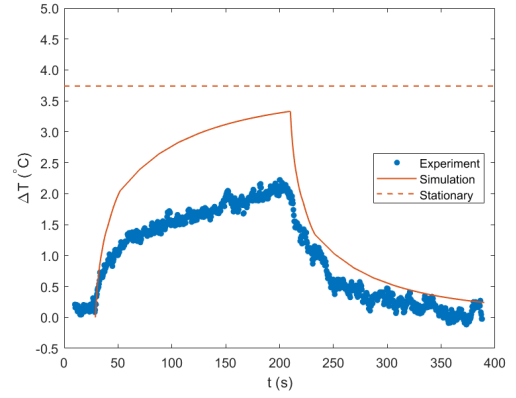


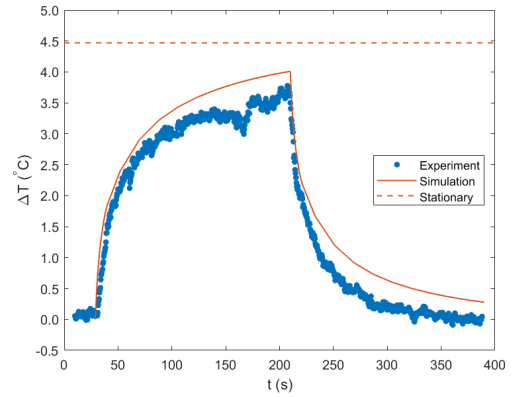
Figure 17: The correlation between the temperature increase measured by the heat camera and the IR thermometer. The correlation coefficient between the two set of data is 0.92. The 95% confidence interval of the fit is presented as dashed lines.



(a) The temperature development from the 761 nm laser. The simulated temperature increase reached 88% of the stationary temperature increase after 3 minutes of laser illumination.

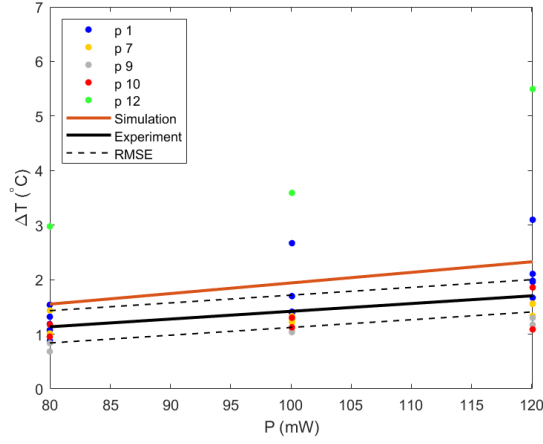


(b) The temperature development from the 937 nm laser. The simulated temperature increase reached 89% of the stationary temperature increase after 3 minutes of laser illumination.

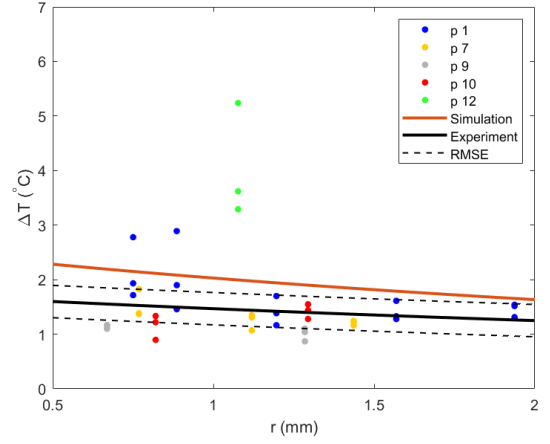


(c) The temperature development from the 971 nm laser. The simulated temperature increase reached 90% of the stationary temperature increase after 3 minutes of laser illumination.

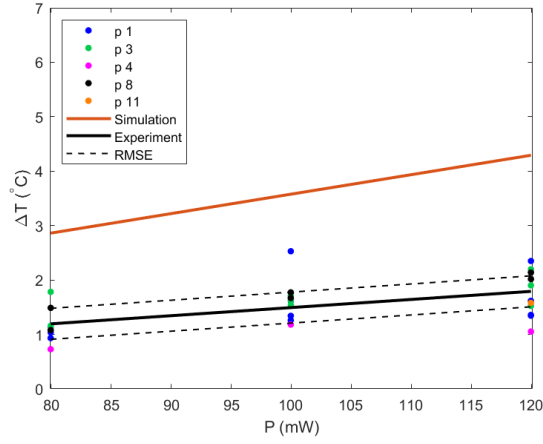
Figure 18: Simulated and experimental temperature development (ΔT) over time (t). The laser is turned on for 3 minutes and then turned off, allowing the forearm to cool down for another 3 minutes. The power is about 100 mW and the radius of the spot is about 1 mm in all cases. The stationary temperature from the simulations are included as a dashed line. The experiments and simulations follows closely for the 761 and 971 nm lasers but differs more for the 937 nm laser.



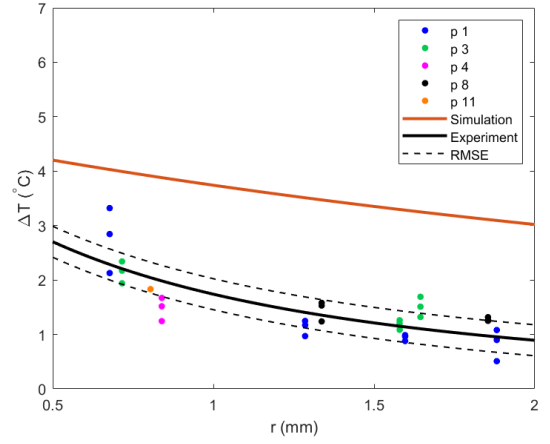
(a) 761 nm laser with $r = 1.2$ mm



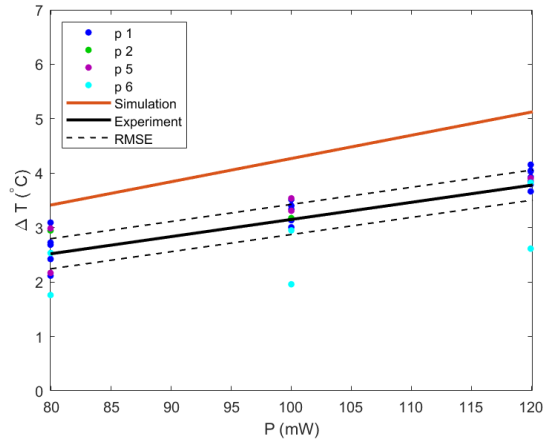
(b) 761 nm laser at $P = 100$ mW



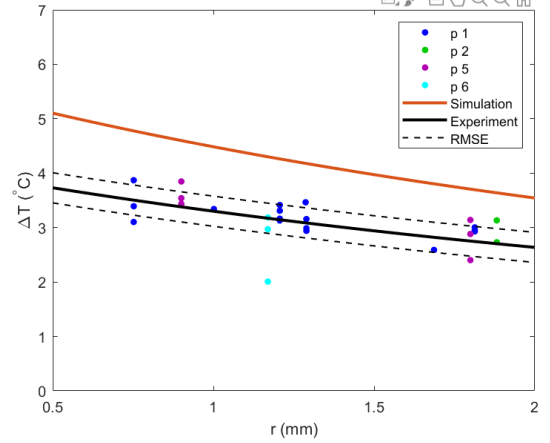
(c) 937 nm laser with $r = 1.2$ mm



(d) 937 nm laser at $P = 100$ mW

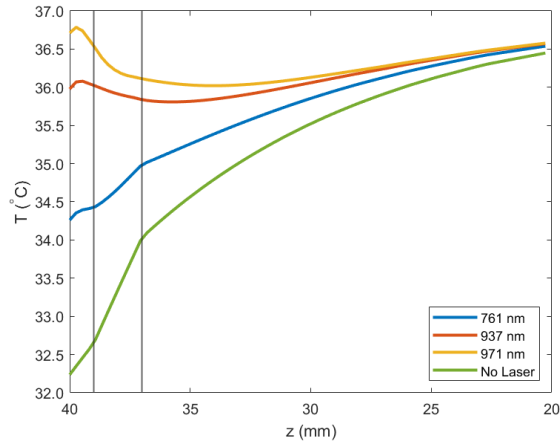


(e) 971 nm laser with $r = 1.2$ mm

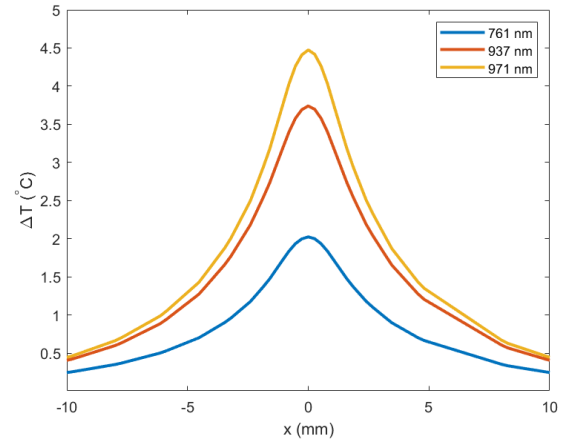


(f) 971 nm laser at $P = 100$ mW

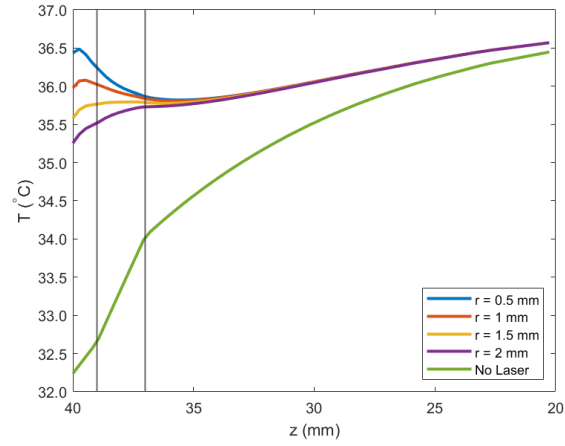
Figure 19: The results from the experiments and simulations plotted together. The dots are the measurement data from the experiments. The model in (18) with coefficients fitted to the simulated data is presented as the red lines whereas the model with coefficients fitted to the experiment data is presented as the black lines. The RMSE of the experiment fit is presented as the dashed lines.



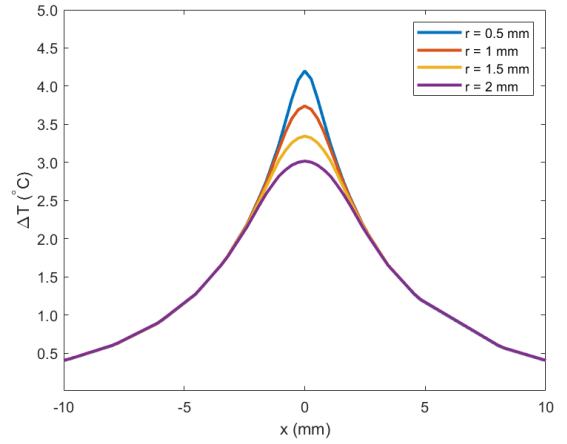
(a) The simulated stationary temperature (T) along the optical axis (z -axis) in the forearm at 100 mW power from the three different wavelengths using a spot radius of 1 mm. The vertical lines denotes the edges of the tissue layers.



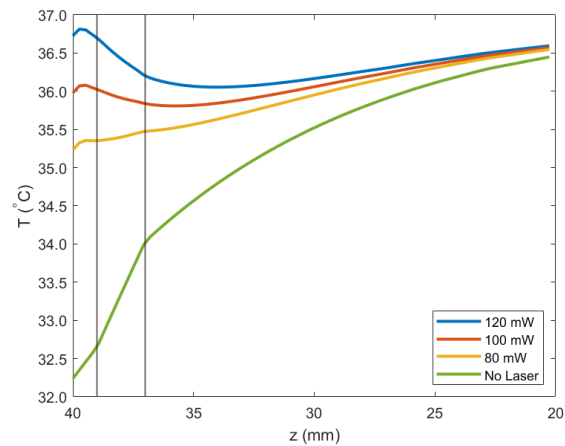
(b) The simulated stationary temperature increase (ΔT) for the skin surface (x -axis at $z = 40$ mm) at 100 mW power from the three different wavelengths using a spot radius of 1 mm



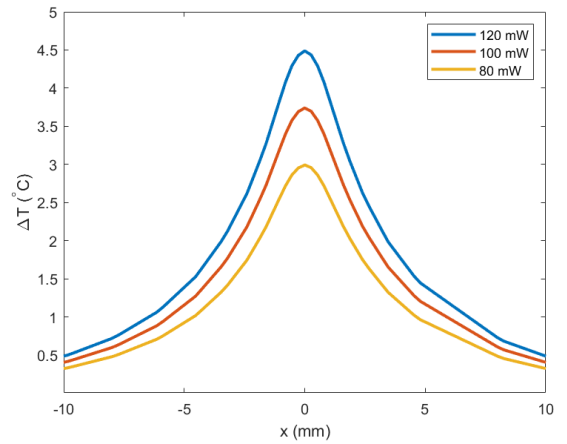
(c) The simulated stationary temperature (T) along the optical axis (z -axis) in the forearm at 100 mW power from the 937 nm laser using spots with different radii. The vertical lines denotes the edges of the tissue layers.



(d) The simulated stationary temperature increase (ΔT) for the skin surface (x -axis at $z = 40$ mm) at 100 mW power from the 937 nm laser using spots with different radii.



(e) The simulated stationary temperature (T) along the optical axis (z -axis) in the forearm at different power levels from the 937 nm laser using a spot radius of 1 mm. The vertical lines denotes the edges of the tissue layers.



(f) The simulated stationary temperature increase (ΔT) for the skin surface (x -axis at $z = 40$ mm) at different power levels from the 937 nm laser using a spot radius of 1 mm

Figure 20

5 Discussion

In Figure 19, it is shown that the experimentally measured temperature increase was generally lower than the simulated temperature increase. It takes a long time to heat up tissue to its stationary value, as illustrated in Figure 18. The simulations after three minutes of illumination only yield about 90% of the actual stationary temperature. Even though the data from the experiments are more noisy, it seems likely that the temperature increase could rise another 10% in them as well.

Another factor explaining the higher temperature increases in the simulations than in the experiments was that the forearms in the experimental study was not completely immobilised. Better conformity between simulations and experiments could potentially have been achieved by strapping the forearms of the volunteers in a comfortable position, using bandages. This was not done since it would deprive the volunteers of some sense of control by not giving them option of instantly terminating the experiment. If a volunteer would have experienced any discomfort they could with this setup, terminate the experiment by just removing their arm from the sample stage. There were, however, no experiments terminated in this way by any of the volunteers. Too tight strapping would also potentially affect the blood flow and hence disturb the natural cooling processes in the tissue.

It is likely that longer illumination times and better immobilisation of the forearms would, on average, have yielded 20 - 30% higher temperature increases than measured in this work. The simulated temperature increases are on average 36% higher than the experimentally measured temperature increases for the 761 and 971 nm laser. These two factors have the potential of reducing the difference between experiments and simulations to just a few percent for these two lasers.

For the 937 nm laser the differences are larger and therefore unlikely to be explained solely by the duration of illumination and the grade of immobilisation. As is seen in Table 11, the model coefficients for the 761 and 971 nm lasers seem to match fairly well with the simulated coefficients in Table 10. This is not the case for the 937 nm laser where both a and r_0 are much lower in the experiments than in the simulations. An explanation for this outcome can be seen in Figure 19d. The experimentally measured temperature increase decays more rapidly for larger spot sizes before plateauing, yielding a more distinctly bent curve compared to the other experiments and the simulations. In order to acquire this shape there has to be a strong inverse square dependence on the radius and consequently r_0 must be small. In order to compensate for the small r_0 value, a must also be small. The shape of the temperature curve from this laser could, at least partially, be explained by the shape of the laser spots shown

in Figure 9. Both the 761 and 971 nm laser spots display a rather elliptic but fairly smooth laser profile. On the other hand the profile of the 937 nm laser features a different geometry with a centralised spot surrounded by an asymmetric halo. The halo gets more distinct at larger laser spots but for very small laser spots it is merged with the centralised spot. As seen in Figure 19d the differences between experiments and simulations for the 937 nm laser using the very smallest laser spots are fairly consistent with the other two lasers. For the larger spots, however, the difference between simulations and experiments for the 937 nm laser is much larger. It is likely that the experimental result for the 937 nm laser would match better with the simulations if using a more symmetric laser spot.

Using the model in (18) with coefficients fitted to the experimental data yields a RMSE of about 0.3 °C for all three wavelengths as seen in Table 11. There is a large number of factors involved in modelling living tissue. These factors vary primarily between people (interpersonal factors) but can also occur within the same person (intrapersonal factors). An example of a factor could be that if a volunteer is getting tired after some measurements the volunteer might find it harder to keep the arm still throughout the whole measurement. Another one could be that the shallow blood perfusion might still be altered between two measurements even though the temperature seems to be back to normal. Table 12 reveals the deviation from the model for each person in the study. Three of the volunteers with light skin displays results that are 20 - 30% below the rest of the studied group. These are person 4, 6 and 9. By studying Table 8 it is revealed that neither gender, age or even small variations in skin tone is a common factor for these three. They are also all illuminated by lasers of different wavelengths. These results reinforces the idea that interpersonal factors, both in optical and thermal properties, can vary a lot between people and that safety margins are always required. Illumination that does not induce any damaging levels of heating for one person could potentially do this for another, seemingly similar person.

The analysis in this project have revolved around laser induced heating from free laser beams, without any physical contact between the light source and the tissue. However, many medical applications uses light sources that are in direct contact with the illuminated tissue surface. These probes disturb the natural cooling mechanisms of the sample surface and hence result in disturbances in the expected temperature increase. By using the FEM model presented in this project, the case of an in-contact probe could with a few modifications be simulated. In a study by Bozkurt and Onaral, it was concluded that the major risk of tissue heating when using LED probes are not the heat induced from the light itself but the heat induced in the semiconductor junction [12]. The efficiency of laser probes are generally not higher than that of LEDs

so the same issue is likely to be apparent for laser probes as well. In order to decrease the heating effects in the tissue from the losses in the semiconductor Bozkurt and Onaral recommended using a thermally insulating layer between the probe and the tissue. Using such an insulating layer will block the heat in the probe from diffusing into the tissue. However, it will also result in higher temperatures within the tissue from the induced light as the heat can not escape at the insulated surface. A suggestion of another solution would be producing the light further away and then transporting the light to the tissue through some sort of fibre. The end attached to the tissue of that fibre should ideally be enlarged so that the resulting spot size on the tissue surface is not very small. If this fibre could be produced in a thermally conducting material it is possible that the fibre could even help cooling the tissue surface. This could be achieved if the fibre is long enough so that the heating from the light source does not spread all the way to the tissue surface. More studies are necessary to further evaluate the heating from probes in direct contact with tissue surfaces.

In the previous study by Ito et al., the laser induced heating from a 789 nm laser is presented as linearly increasing as a function of the irradiance [14]. Their results are in principal reinforced by the outcome of this work, as they only varied the laser power. However, the irradiance is also depending on the area of the illuminated spot and the results from this work does not suggest any inverse proportionality between the temperature increase and the area of the laser spot. The dependence of the irradiance (intensity) is presented in Figure 16 where the non-linear dependence between the temperature increase and the intensity when varying the spot size is easily seen in the simulated data (top). Even in the experimentally measured data (bottom) there does not seem to be any linear dependence, even if the results are too noisy for any certain conclusions to be drawn. In the study by Ito et al., they also measured a temperature increase of about 0.1 °C per mW for their 789 nm GaAs laser with a spot size of about 1 mm². This is higher than the simulated heating in this work and more than double the experimentally measured heating. However, in their report it is stated that they probably overestimated the real temperature increases by about a factor 3, because of direct absorption in the thermocouple. Taking this factor in consideration the outcomes of this work matches well with that of Ito et al.

In the study by Simpson et al., it was concluded that the absorption coefficient is higher in more pigmented skin [25]. A consequence of a higher absorption coefficient should logically be higher temperature increases from laser illumination. The induced heating on more pigmented skin illuminated by 633 nm laser was also higher in the study by Pålsson et al. [13]. The results from this work suggest that the heating of more pigmented

skin, classified as Fitzpatrick type 5, is higher than for the heating for lighter skin of type 1-3. This is just as expected based on the previous works presented above. However, the heating of the more pigmented skin in this work, illuminated by the 761 nm laser, is even higher than in the study by Pålsson et al. While they measured almost doubled temperature increases on more pigmented skin, the heating in this work was closer to three times higher than that of lighter skin. The larger difference at the wavelengths used in this work, even though the melanin absorption has decreased, can probably be explained by that the blood absorption has decreased even more, which is seen in Figure 2. Clearly, further similar studies needs to be performed on the laser induced heating of a larger population of people with skin of Fitzpatrick type 4-6 in order to gain more knowledge of how much the heating differs between people. As this study was performed in the late winter on untanned volunteers it is possible that performing the same study on the same volunteers during the summer would yield slightly higher temperatures, as the participants would be more tanned.

The measured temperature increase from laser illumination of mucosa varied more than on the forearm. Holding the lower lip in place throughout the whole measurement duration proved difficult as it was slippery and got dry after some time. The lack of melanin was a factor that could potentially reduce the induced temperature increase but the higher amount of superficial veins and high water content was other factors that had the potential to increase it. There were large deviations between the volunteers and especially on the volunteer illuminated by the 761 nm laser the induced heating seemed to be possibly a little higher than what was measured on the forearm as it was 30% higher than the average of the forearm measurements. The difference was however not large enough to prove whether there are any real difference between the laser induced heating of a forearm and mucosa.

5.1 Spatial temperature increase

From the simulations, the temperature in the whole forearm geometry was extracted. Only the peak surface temperatures could be compared to any experimental data but the rest can still be interesting on its own for analysing how heat spread in tissue. These plots for varied wavelength, spot size and power are shown in Figure 20.

The simulation results from Figure 20c and 20d suggests that changing the laser spot size over a constant power only affect the temperature close to the tissue surface. Deeper within the tissue the light is so scattered that the source geometry have very low impact on the temperature increase. The fact that multiple photon-scattering reduces the impact of the source term is the basis for diffusion theory for light transport [15]. This theory is naturally not founded on the thermal aspects of illumina-

tion but the photon flux. However, it is interesting that this phenomena is still very apparent even when simulating photon induced-heating. Logically, some broadening of the slopes of the surface temperature profiles in Figure 20d would be expected for the larger laser spots. The broadening is motivated by that the same amount of energy is still deposited in the tissue but over a larger area. The higher temperature difference for smaller laser spots should also result in more surface cooling and consequently less total energy stored in the tissue. If there is any broadening of the slopes with larger spot sizes the broadening is too small to be seen in these figures.

In all the simulated cases the temperature is higher in the core of the skin layer than on the skin surface, as seen in the left plots of Figure 20. The largest contribution to this phenomenon is the baseline temperature in the forearm that increase faster with depth than the induced heating decays. The impact on the surface from the convective and radiative cooling is probably also contributing factors. There are no simulated cases where the temperature increase from the baseline temperature is higher inside the tissue than on the tissue surface. There are furthermore no simulated cases where the temperature difference is higher than 0.2°C inside the tissue than on the surface. In all the simulated cases shown in Figure 20, the skin temperature is below 37°C and consequently the core body temperature is higher. In these cases there are no risk of thermal damage. However, if the temperature on the skin surface is above 37°C there is a risk that the temperature might be even slightly higher a little deeper inside the skin, which should be taken in consideration. In the simulations of this project, the melanin content is distributed over a thicker skin layer than in real tissue. Instead of being distributed in a less than $100\text{ }\mu\text{m}$ thick outer epidermis layer, it is spread out in the whole 1 mm thick skin layer. This is a detail that probably makes the effect more apparent in this work than in real tissue. As mentioned in chapter 3.1 the resolution of the simulated grid could not be fine enough for distinguishing the epidermis because of hardware limitations.

There are therapeutic applications where tissue below the outmost skin layer is heated more than the skin layer itself, using laser techniques. An example is the treating of port wine stains [15]. In this example, the abnormally high blood concentrations just below the skin surface is utilised for its high absorption of green light. The high local absorption of the green laser light increase temperature in the port wine stain layer, damaging the blood vessels that are causing the discoloration while leaving surrounding tissue relatively unharmed.

It is relatively easy to measure the surface temperature and based on those measurements adjust the power levels to not risk damage the tissue surface. However, it is much harder to measure the temperatures deeper within

the tissue. The tendency of slightly higher temperatures a little deeper within the tissue than on the tissue surface is an interesting phenomenon to study even though it does not seem to be a critical safety issue for NIR light, based on the results of this work. If one wants to assure that the temperature stays below a threshold value everywhere in the tissue, this phenomenon has to be considered. This especially when illuminating tissues with a higher baseline temperature, where the safety margins are lower, such as the torso.

5.2 Model for skin surface heating

In this section the model in (18) for predicting the surface temperature is discussed. The model is derived in this work and tested on the results from both the simulations and experiments. It works well for minimising the RMSE of the experimental data. Compared to a linear combination the model improves the RMSE by about 10% for the two lasers with higher wavelengths. Even for the 761 nm laser the fit is improved by a few percent.

As mentioned in the introduction the second goal of the project was creating a model for predicting the resulting heating from laser illumination. This in order to minimise risk of any thermal damage from medical devices using continuous lasers. The main purpose of the model is hence using it for predicting the resulting surface heating for wavelengths, powers and spot sizes that are not necessarily included, but are in the neighbourhood of the ones used in the project. The result of the model plotted over a larger span of powers and spot sizes with coefficients from the simulations are shown in Figure 21. By using the coefficients from the simulations in Table 10, predictions that are close to the true stationary heating should be acquired for illumination on light skin. These predictions does not include any safety margin which need to be added when using the model. Based on the results in this work, if using the model on more pigmented skin the expected temperature increase should be multiplied by about a factor 3.

The model predicts a few things. Firstly, it predicts that by decreasing the spot size to a very small area (e.g. less than 1 mm^2) the temperature increase should reach some value only depending on the power (P) and a smallest possible light distribution due to scattering and absorption. The derivation of the model assumes this smallest possible uniform light distribution to a half sphere with a radius r_0 . However, the true fluence rate from a laser source is not evenly distributed, as seen in Figure 5. Logically, there should be parts close to the illuminated skin surface where the high fluence rate gives rise to potentially even higher temperature increases than the ones measured and simulated in this work. This is not something that is supported by the results though, neither from the simulations nor the experiments. Instead the idea of

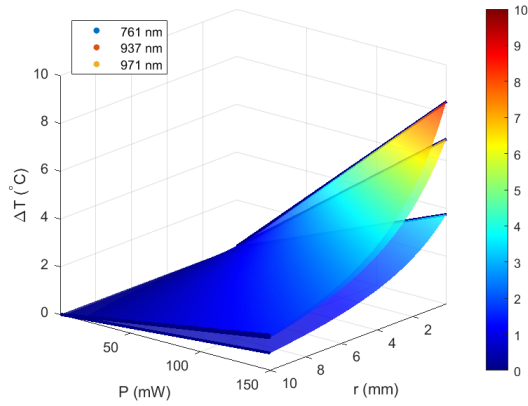


Figure 21: The model for laser induced surface heating from equation (18) with the coefficients fitted from the simulations, presented in Table 10. The model is plotted for powers ranging between 0 and 150 mW and for radiuses of the laser spot ranging between 0.1 and 10 mm. The heating from the 761 nm laser is in the bottom surface, the 937 nm laser in the middle and the 971 nm laser is on the top.

a smallest possible distribution, as is used in the model derivation, seem to fit these results better. It can be discussed whether these results are due to the roughness of the grid in the simulations and the resolution of the two thermal measurement devices. The true thermal response of tissue illuminated at very small spot sizes is left as an open question in this work.

The model also predicts how the resulting surface heating should decrease when the spot size is increased. A potential risk factor that must be taken in consideration of when using larger laser spots is that the temperature deeper inside the tissue can be higher than at the tissue surface. When increasing the spot size the same amount of energy is still deposited in the tissue but over a larger surface area. Deeper within the tissue the impact of the source geometry is low as discussed earlier so the temperatures there will be the same as with a smaller spot size. Based on the results from the simulations in this work this is however not a major risk factor as there are no cases where the temperature inside the tissue is more than 0.2 °C higher than at the surface.

For the power dependence, the model predicts a linear increase in heating when increasing the power. This linear correlation seems very strong both in the simulations and the experiments and also follows the results of previous works. The volumetric heat production from equation (10) is the distribution of energy over a volume. The shape of the distribution ($\mu_a d_\phi$) is independent of the power as the photons are independent of one another. Non-linear interactions of light within tissue occur but only at very high powers, making them irrelevant for this project [15]. The linear dependence between the heating

and power is expected to decrease slightly at higher levels of heating as the surface cooling processes are depending on the temperature difference at the tissue surface.

Another key issue is how well this model works for other wavelengths than the three presented in the project. A property of the wavelengths selected, as can be seen in Figure 2, is that they are all located at local maximum of the absorption for many of the principal chromophores in the body. The resulting laser-induced heating from wavelengths close to the selected ones are therefore expected to be similar or even slightly lower than for the ones in the project. Using lasers with wavelengths of 740 or 780 nm should hence not induce higher temperatures than at 761 nm using the same power levels. However, scattering is also an important factor. Scattering increases for shorter wavelengths which could result in larger temperature increases in the superficial skin layers and must be taken into account.

For wavelengths further away in the spectrum, this work can be interesting as a pointer of what levels of laser-induced heating to expect. Outside the optical window between 700 and 1100 nm, much larger temperature increases are expected as the absorption increases rapidly. In these regions the coefficients presented in this work are of no use anymore but the derivation of the model should still be as valid. Further studies could be performed on testing the model in other wavelength regions and extracting coefficient values that are useful for those wavelengths.

A way of making the model more versatile would be expressing the coefficients a and r_0 in already known parameters. Already in the model derivation r_0 is assumed to be depending on the absorption and scattering of the media. It is likely that r_0 could be expressed in terms of μ_a and μ_s . For larger μ_a , r_0 should logically decrease as the photons get absorbed faster. The dependency of μ_s is not as straight-forward but assuming that the media is scattering dominated, an increased μ_s should mean that it is more difficult for photons to spread deeper inside the media which also should decrease r_0 . The coefficient a is probably also somewhat depending on optical parameters. However, in the derivation it is presented as inversely depending on the thermal conductivity (k). Another factor that also seem to be of importance for a is the reflectance (R). The idea is based on the observation that a for the 761 nm laser is much lower than for the other two lasers while this laser also features a much higher reflectance, as shown in Figure 12. With a higher reflectance there is a lower amount of energy deposited in the tissue so increasing R should logically decrease a .

5.3 Method discussion

The measurements from the heat camera was the data mainly used in the analysis. The reason was that it recorded the temperature over a large area, allowing both spatial analysis and subtraction of background noise from an unheated spot on the arm. It also did not require perfect aim on the laser illuminated spot as the peak heated pixel could easily be found afterwards during data analysis. The aim of the IR thermometer had to be adjusted frequently and in some measurements it slightly missed the peak of the laser induced heat spot resulting in less continuity than from the heat camera. As seen in Figure 17, most data still correlates well between the IR thermometer and the heat camera. There are a few cases where the IR thermometer actually reports a higher temperature increase than the heat camera. Those measurements was generally acquired when using a very small laser spot, as the smallest resolution of the IR thermometer is better than that of the heat camera. However, since it only captured data from a single point there was no baseline data acquired that could be used in order to suppress noise. An example is that there seemed to be a tendency for the temperature of the forearm to drop naturally one or two tenths of a °C after a few minutes of being at rest on the sample platform. This was subtracted in the heat camera data but is still influencing the IR thermometer data. However, for analysing stationary *in-vitro* samples the IR thermometer is probably more useful than the heat camera because of its higher resolution and sampling rate.

Another method that could have been used for measuring temperature in the project is using a thermocouple probe. This was done for example in the study by Ito et al. and yields the possibility of measuring temperature deeper inside the tissue [14]. A main drawback of this method, also reported by Ito et al., is that thermocouples have a high tendency of directly absorbing NIR laser light, resulting in measured temperatures much higher than the true tissue temperatures. Inserting a thermocouple into living tissue is also a type of operation requiring both expertise and ethical approval. However, a thermocouple with low absorption of NIR light could be useful in studies performed on tissue phantoms.

Living tissue is a medium where the temperature is actively regulated to pleasant levels. Thermal regulation of the body is controlled by the hypothalamus [43]. Sweating is one of these regulating process that contributes in cooling living tissue. This process was intentionally excluded from the model as it is difficult to model and its contribution was assumed to be low for the temperature levels of this project [35]. For very local heating, cooling effects can be achieved by regulation of the blood perfusion [15]. However in the study by Ito et al. the cooling effects from blood perfusion was negligible [14]. In the simulations of this project the blood perfusion rate

was set to a constant value, independent of any external impacts. More studies on local temperature regulating processes in living tissue, such as the contribution from blood perfusion, could provide tools for generating even better models of thermal regulations in laser illuminated tissue.

The skin surface temperature development over time, both for the simulations and experiments, are shown in Figure 18. Both the heating and cooling seem to match well between the simulations and experiments for the 761 and 971 nm lasers. This suggests a good conformity between the FEM model of tissue heating and the experiments. However the temperature development for the 937 nm laser does not match as well. It seems that much more energy is deposited in the tissue per time unit in the simulations than in the experiments. Previously, the impact of the asymmetric laser spot in the case for the 937 nm laser has been discussed but there could be more contributing factors. From Figure 18b, it seems like less energy is deposited in the tissue in the experiments than in the simulations. The volumetric heat production term in equation (10) is extracted from the MC simulation and is only depending on the optical parameters of the media. In the review by Jacques et al., it is shown that measured optical parameters generally features a very high deviation between different studies, even on the same type of tissue [17]. In the review, the standard deviation of the scattering coefficients for many types of tissue are about half the mean value. Consequently, the models used for extracting the absorption (6) and scattering (7) coefficients feature the same high deviations.

The quality of the output from the MC simulation for this application can also be questioned. MCX was originally tested versus the diffusion equation [30] but later studies also tested it on experimental data [44, 45]. The experimentally measured quantities correlated well with the simulations in these works. However, the studied quantities were the emitted photons scattered out of the media and not the thermal interactions within the media. No such tests for experimental validation of MCX was found. However, such a test could be conducted using experiments on tissue phantoms with known optical and thermal properties. The experiment could be performed with the same method as the study on healthy volunteers in this work.

The model used for extracting the absorption coefficient is presented in equation (6). The main chromophores for human tissue in the NIR spectra are blood, water melanin and fat. However, in the paper presenting this model Jacques states that roughly 30% of the volume fraction consists of fibrous materials [17]. Collagen is the most abundant fibrous protein in our bodies and it is in a more recent study by Sekar et al., shown to have significant absorbing properties of NIR light [46]. It is possible that the

absorption coefficient model could be improved slightly by also including the collagen spectra.

The experiments in this study were performed without immobilising the arms of the volunteers. A way of potentially improving the consistency in the experiment results would be using a suitable U-shaped cradle. The arms would be placed in this cradle, reducing movement without the use of straps. Using laser profiles with better symmetry would also be a simple way of potentially improving the experiment data. The laser profiles used, presented in Figure 9, featured different geometries resulting in an uneven spread of the energy over the illuminated surface. This seems especially apparent for the 937 nm laser. A way of improving the output profile could be collecting the light in an optical fibre and placing the other end of the fibre facing the forearm. This method was tried but proved unsuitable for the setup in this project as the magnitude of the power lost when focusing the beam at the fibre end was too high.

It is possible that the white paper that was illuminated in the experiments for extracting the effective area of the laser spot, slightly increased the spot size because of its highly scattering nature. If this is the case the size increase was too small to be distinguished when comparing with the laser profile acquired by direct illuminating of a larger CCD detector. The method with the illuminated paper was practical as it did not require any rearrangements to fit in the setup as was the case when using a larger detector.

In a study by Mendenhall et al., the reflectance of light skin was measured to about 50 - 60% for the wavelength used in this project [47]. In the output of the MC simulations the fraction of energy that was absorbed in the media is given. The fraction not absorbed in the media is reflected, either on the surface or diffusely. These reflected fractions are presented in Figure 12. The reflectance from the simulations of the 937 and 971 nm lasers are very close to the values measured experimentally by Mendenhall et al. For the 761 nm laser the simulated reflectance in this work is about 5-10% higher than their measured values.

5.4 Ethical aspects

Throughout this work the safety of everyone participating has been of utmost importance. The powers used in the project were first tested on chicken meat and then carefully on the author by carefully running numerous experiments with slowly ramped-up power. For ethical purposes the forearms of the volunteers were not immobilised as they were illuminated, something that could have slightly affected the quality of the measurements but something that was considered the best way of procedure. During the measurements there were no volunteer that with certainty

sensed any heating of the illuminated spot on their forearm. In the study by Rhoon et al., it was concluded that no thermal damage can occur in tissue below temperatures of 39 °C [29]. Their paper has been an important guideline for this project as it provided a safe threshold value for the heating. It was decided, based on their paper, that no measurements resulting in any temperatures close to reaching 39 °C should be performed. In a few cases during the study, the measured temperature reached just above 37 °C. With possible measurement offsets and the uncertainty of how the temperature is distributed inside the tissue, higher temperatures than that was not desirable.

Despite the negligible risk of thermal damage to the skin, the hazard of eye damage was also an important issue. Everyone participating in any of the experiments has been provided with protective glasses with at least OD6 in the specific wavelength region. These glasses had to be worn at all times when any laser was in operation in the lab.

It is also very important that anyone using any of the outcomes of the work, for example the model in (18), are aware of the hazards of lasers. It is up to the user of this work to make sure that no potentially harmful situations occur. The outcomes of this work can serve as guidance but they are useless without good judgement of the user.

6 Conclusion

In this work it has been concluded that laser-induced heating is linearly depending on the laser power. It is furthermore concluded that the heating is non-linearly depending on the inverse square of the radius of the laser spot. By combining these dependencies a model that predicts the resulting surface heating for wavelengths, powers and spot sizes in the neighbourhood of the ones used in the project is produced. Based on the results it is furthermore concluded that there is no linear correlation between the intensity of the laser illumination and the surface heating for the wavelengths, power levels and spot sizes used in this work.

In order to avoid thermal damage in laser illuminated tissue the model in (18) with the simulated coefficients in Table 10 can be used. This model predict the surface heating of light skin within the optical window. The absolute temperature of any tissue should not be allowed to reach above 39 °C [29]. In order to effectively decrease the laser-induced heating, low power levels and illumination with larger laser spots are recommended. Illumination at wavelengths near the ones used in the project should have similar thermal properties as the one presented in this work. Extra caution is required when using powers higher than the 120 mW experimentally tested in the project or when using illuminated spots smaller than 1 mm². The temperature increase deeper in the tissue, as visualised in the left plots of Figure 20, should also be taken into account as these are less depending on the size of the laser spot. If illuminating more pigmented skin, the expected temperature increase should be multiplied by about a factor 3. The model does not include any safety margins so these also need to be added as the results can be highly varying between seemingly similar people. Generally, a high level of caution is necessary when working with lasers and especially illuminating living tissue. It is up to the user of this work to use their own best judgement to not expose anyone to any situations where potentially harmful doses of illumination can be deposited.

The outcomes of this work are meant to be used for aiding the development of non-invasive clinical devices that utilise the tissue optical window in the near infrared range for diagnostics or monitoring.

7 References

- [1] S. I. Hajdu. “A note from history : The first use of the microscope in medicine”. In: *Annals of Clinical Laboratory Science* 32.3 (2002), pp. 309–310.
- [2] D. Jocham, H. Stepp, and R. Waidelich. “Photodynamic diagnosis in urology : State-of-the-Art”. In: *European Urology* 53 (2008), pp. 1138–1150. DOI: 10.1016/j.eururo.2007.11.048.
- [3] T. Dougherty and S. Schwartz. “Photodynamic therapy for cancer skin of mice”. In: *Nature Reviews Cancer* 3 (2003), pp. 380–387. DOI: 10.1038/nrc1070.
- [4] M. F. Yanik, H. Cinar, H. N. Cinar, A. D. Chisholm, Y. Jin, and A. Ben-Yakar. “Functional regeneration after laser axotomy”. In: *Nature* 432 (2004), p. 822.
- [5] Z. Turani, E. Fatemizadeh, T. Blumetti, S. Daveluy, A. F. Moraes, W. Chen, D. Mehregan, P. E. Andersen, and M. Nasirivanaki. “Optical radiomic signatures derived identification of melanoma”. In: *Proceedings of Spie*. 2019. DOI: 10.1117/12.2526624.
- [6] L. Shi, L. A. Sordillo, A. Rodríguez-contreras, and R. Alfano. “Transmission in near-infrared optical windows for deep brain imaging”. In: *Journal of Biophotonics* 9.1-2 (2016), pp. 38–43. DOI: 10.1002/jbio.201500192.
- [7] J. W. Severinghaus and Y. Honda. “History of blood gas analysis. VII. Pulse oximetry”. In: *Journal of Clinical Monitoring* 3.2 (1987).
- [8] S. Svanberg. “Gas in scattering media absorption spectroscopy – from basic studies to biomedical applications”. In: *Laser Photonics Reviews* 796.5 (2013), pp. 779–796. DOI: 10.1002/lpor.201200073.
- [9] D. J. Gallacher, K. Hart, and S. Kotecha. “Common respiratory conditions of the newborn”. In: *Breathe* 12.1 (2016), pp. 30–42.
- [10] D. G. Sweet, G. Greisen, and H. L. Halliday. “European consensus guidelines on the management of respiratory distress syndrome – 2019 update”. In: *Neonatology* 115 (2019), pp. 432–450. DOI: 10.1159/000499361.
- [11] P. Lundin, E. K. Svanberg, L. Cocola, M. L. Xu, G. Somesfalean, S. Andersson-engels, J. Jahr, V. Fellman, K. Svanberg, and S. Svanberg. “Noninvasive monitoring of gas in the lungs and intestines of newborn infants using diode lasers : feasibility study”. In: *Journal of Biomedical Optics* 18.12 (2013). DOI: 10.1117/1.JBO.18.12.127005.

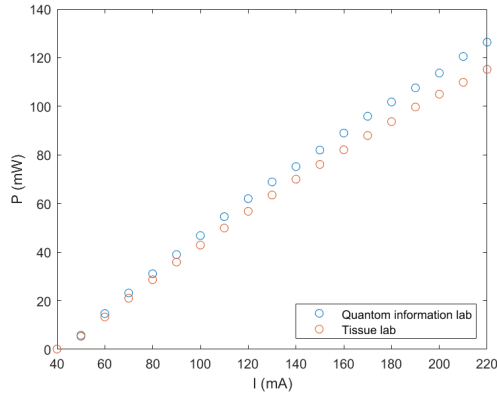
- [12] A. Bozkurt and B. Onaral. "Safety assessment of near infrared light emitting diodes for diffuse optical measurements". In: *BioMedical Engineering OnLine* 3.9 (2004).
- [13] S. Pålsson, L. Gustafsson, N. Bendose, M. Soto Thompson, S. Andersson-Engels, and K. Svanberg. "Kinetics of the superficial perfusion and temperature in connection with photodynamic therapy of basal cell carcinomas using esterified and non-esterified 5-aminolaevulinic acid". In: *British Journal of Dermatology* 148 (2003), pp. 1179–1188.
- [14] Y. Ito, P. Kennan, R. E. Watanabe, and H. Koizumi. "Assessment of heating effects in skin during continuous wave near infrared spectroscopy". In: *Journal of Biomedical Optics* 5.4 (2000), pp. 383–390.
- [15] A. J. Welch and M. J. Van Gemert. *Optical-thermal response of laser-irradiated tissue*. Second edition. Springer, 2011.
- [16] S. Svanberg. *Atomic and molecular spectroscopy*. 4th. Lund: Springer, 2004.
- [17] S. L. Jacques. "Optical properties of biological tissues : a review". In: *Physics in Medicine & Biology* 58 (2013), pp. 37–61. DOI: 10.1088/0031-9155/58/11/R37.
- [18] S. Prahl and S. Jacques. *A compendium of tissue optical properties*. 2012. URL: <https://omlc.org/index.html>.
- [19] V. Tuchin. *Tissue optics: Light scattering methods and instruments for medical diagnostics*. Third edition. Bellingham, Washington USA: Society of Photo-Optical Instrumentation Engineers (SPIE), 2015.
- [20] K. Das, T. Yuasa, I. Nishidate, H. Funamizu, and Y. Aizu. "Simulated reflectance spectra and point spread functions in database constructed by moderate grouping of nine layers in skin model". In: *Optical Review* (2020). ISSN: 1349-9432. DOI: 10.1007/s10043-020-00579-8.
- [21] E. Salomatina, B. Jiang, J. Novak, and A. N. Yaroslavsky. "Optical properties of normal and cancerous human skin in the visible and near-infrared spectral range". In: *Journal of Biomedical Optics* 11.6 (2006). DOI: 10.1117/1.2398928.
- [22] S. E. Cameron, P. A. D'Angelo, M. A. Auerbach, and J. W. Ramsay. "In vivo ultrasonic measures of skin layer thicknesses at various body locations and postures". In: *Proceedings of Spie* 10580.March 2018 (2018). DOI: 10.1117/12.2293592.
- [23] K. Hwang, H. Kim, and D. J. Kim. "Thickness of skin and subcutaneous tissue of the free flap donor sites: a histologic study". In: *Microsurgery* 36.1 (2015). DOI: 10.1002/micr.
- [24] S. Sachdeva. "Fitzpatrick skin typing: Applications in dermatology". In: *Indian J Dermatol Venereol Leprol* 75.1 (2009).
- [25] C. R. Simpson, M. Kohl, M. Essenpreis, and M. Cope. "Near-infrared optical properties of ex vivo human skin and subcutaneous tissues measured using the Monte Carlo inversion technique". In: *Physics in Medicine & Biology* 43 (1998), pp. 2465–2478.
- [26] J. Leal, H. D. C. Smyth, and D. Ghosh. "Physicochemical properties of mucus and their impact on transmucosal drug delivery". In: *International Journal of Pharmaceutics* 532.1 (2017), pp. 555–572. ISSN: 0378-5173. DOI: 10.1016/j.ijpharm.2017.09.018. URL: <http://dx.doi.org/10.1016/j.ijpharm.2017.09.018>.
- [27] A. Ahad, S. Tandon, A. Kaur Lamba, F. Faraz, P. Anand, and A. Aleem. "Diode laser assisted excision and low level laser therapy in the management of mucus extravasation cysts: A case series". In: *Journal of in Lasers Medical Sciences* 8.3 (2017), pp. 155–159. ISSN: 2008-9783. DOI: 10.15171/jlms.2017.28. URL: <http://dx.doi.org/10.15171/jlms.2017.28>.
- [28] P. S. Yarmolenko, E. Jung Moon, C. Landon, A. Manzoor, W. Hochman, Daryl, L. Viglianti, Benjamin, and W. Dewhirst, Mark. "Thresholds for thermal damage to normal tissues : An update". In: *NIH Public Access* 27.4 (2011), pp. 320–343. DOI: 10.3109/02656736.2010.534527.Thresholds.
- [29] G. C. V. Rhoon, T. Samaras, P. S. Yarmolenko, M. W. Dewhirst, E. Neufeld, and N. Kuster. "CEM43 ° C thermal dose thresholds : a potential guide for magnetic resonance radiofrequency exposure levels ?" In: *European Radiology* 23 (2013), pp. 2215–2227. DOI: 10.1007/s00330-013-2825-y.
- [30] Q. Fang and D. A. Boas. "Monte Carlo simulation of photon migration in 3D turbid media accelerated by graphics Processing Units". In: *Opt. Express* 17.22 (Oct. 2009), pp. 20178–20190. DOI: 10.1364/OE.17.020178. URL: <http://www.opticsexpress.org/abstract.cfm?URI=oe-17-22-20178>.
- [31] L. Wang, S. L. Jacques, and L. Zhengb. "MCML - Monte Carlo modeling of light transport in multi-layered tissues". In: *Computer methods and programs in biomedicine* 47 (2 1995), pp. 131–146. DOI: 10.1016/0169-2607(95)01640-F.

- URL: <https://www.sciencedirect.com/science/article/pii/S016926079501640F>.
- [32] S. A. Filatova, I. A. Shcherbakov, and V. B. Tsvetkov.
“Optical properties of animal tissues in the wavelength range from 350 to 2600 nm”.
In: *Journal of Biomedical Optics* 22.3 (2017).
DOI: 10.1117/1.JBO.22.3.035009.
- [33] I. V. Meglinski and S. J. Matcher. “Computer simulation of the skin reflectance spectra”.
In: *Computer Methods and Programs in Biomedicine* 70 (2002), pp. 179–186.
- [34] N. Ottosen and H. Petersson.
Introduction to the finite element method.
Harlow: Pearson Education, 1992, pp. 1–10.
- [35] C. Stureson and S. Andersson-Engels.
“A mathematical model for predicting the temperature distribution in laser-induced hyperthermia. Experimental evaluation and applications”. In: *Physics in Medicine & Biology* 40 (1995), pp. 2037–2052.
DOI: 10.1088/0031-9155/40/12/003.
- [36] J. Chalupský, J. Krzywinski, L. Juha, V. Hájková, J. Cihelka, T. Burian, J. Gaudin, A. Gleeson, M. Jurek, A. R. Khorsand, D. Klinger, H. Wabnitz, R. Sobierajski, M. Störmer, K. Tiedtke, and S. Toleikis.
“Spot size characterization of focused non-Gaussian X-ray laser beams”. In: *Optics Express* 18.26 (2010), pp. 27836–27845.
DOI: 10.1117/1.OE.53.12.122513.
- [37] A. Stratan, A. Zorila, L. Rusen, and G. Nemes.
“Measuring effective area of spots from pulsed laser beams”.
In: *Optical Engineering* 53.12 (2014).
DOI: 10.1117/1.OE.53.12.122513.
- [38] P. Hasgall, F. Di Gennaro, C. Baumgartner, E. Neufeld, B. Lloyd, M. Gosselin, D. Payne, A. Klingeböck, and N. Kuster.
IT’IS Database for thermal and electromagnetic parameters of biological tissues. Version 4.0.
IT’IS foundation, 2018.
- [39] E. Calzia, Z. Iványi, and P. Radermacher.
“Determinants of blood flow and organ perfusion”.
In: *Functional hemodynamic monitoring. update in intensive care and emergency medicine*.
Ed. by M. R. Pinsky and D. Payen. vol 42.
Berlin, Heidelberg: Springer, 2005.
DOI: https://doi.org/10.1007/3-540-26900-2_3.
- [40] G. Havenith, I. Holme, and K. Parsons. “Personal factors in thermal comfort assessment : clothing properties and metabolic heat production”.
In: *Energy and Buildings* 34 (2002), pp. 581–591.
- [41] C.-y. Yu, Y.-h. Lo, and W.-k. Chiou.
“The 3D scanner for measuring body surface area : a simplified calculation in the Chinese adult”.
In: *Applied Ergonomics* 34 (2003), pp. 273–278.
DOI: 10.1016/S0003-6870(03)00007-3.
- [42] F. J. Sanchez-marin, S. Calixto-carrera, and C. Villaseñor-mora. “Novel approach to assess the emissivity of the human skin”.
In: *Journal of Biomedical Optics* 14.2 (2009).
DOI: 10.1117/1.3086612.
- [43] I. Campbell.
“Body temperature and its regulation”.
In: *Anaesthesia & Intensive Care Medicine* 9.6 (2008), pp. 259–263.
- [44] R. Yao, X. Intes, and Q. Fang.
“Generalized mesh-based Monte Carlo for widefield illumination and detection via mesh retessellation”.
In: *Biomedical Optics Express* 7.1 (2015).
DOI: 10.1364/BOE.7.000171.
- [45] J. Chen, Q. Fang, and X. Intes. “Mesh-based Monte Carlo method in time-domain wide field fluorescence molecular tomography”.
In: *Journal of Biomedical Optics* 17.10 (2012).
DOI: 10.1117/1.JBO.17.10.106009].
- [46] S. K. V. Sekar, I. Bargigia, A. D. Mora, P. Taroni, A. Ruggeri, A. Tosi, A. Pifferi, and A. Farina.
“Diffuse optical characterization of collagen absorption from 500 to 1700 nm”.
In: *Journal of Biomedical Optics* 22.1 (2017).
DOI: 10.1117/1.JBO.22.1.015006.
- [47] M. J. Mendenhall, A. S. Nunez, and R. K. Martin.
“Human skin detection in the visible and near infrared”. In: *Applied Optics* 54.35 (2015).

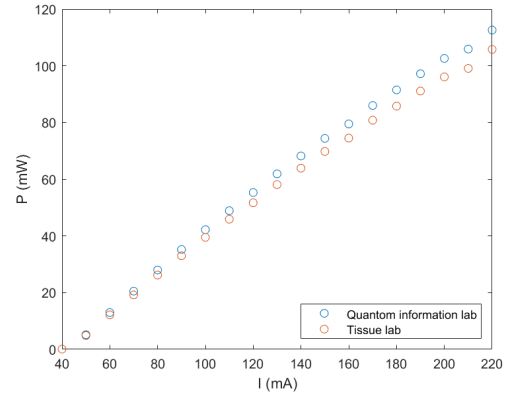
8 Appendix

8.1 Appendix A - Power meter calibration

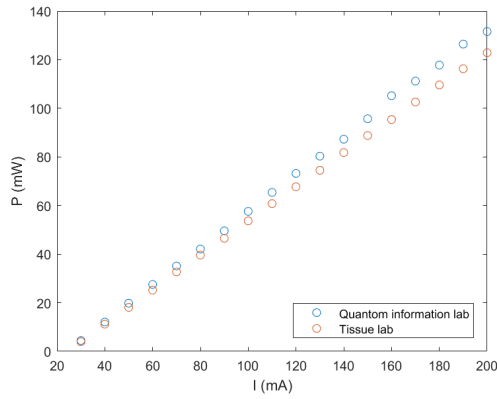
The power meter in the tissue spectroscopy lab required calibration. A more recently calibrated similar power meter was loaned from the quantum information lab in order to do so. The measured output power as a function of the laser diode drive current for the two power meters and each diode laser is presented in Figure 22. The differences are plotted in Figure 23 where a calibration curve is extracted.



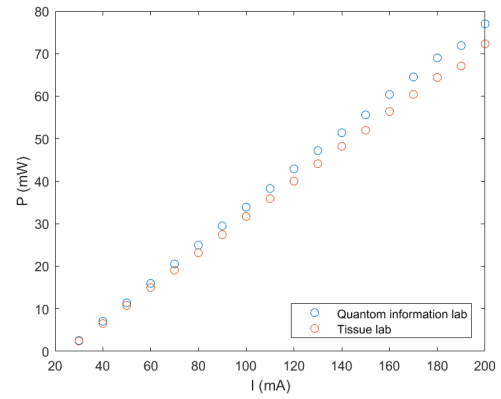
(a) Power measured close to the 761 nm laser diode surface.



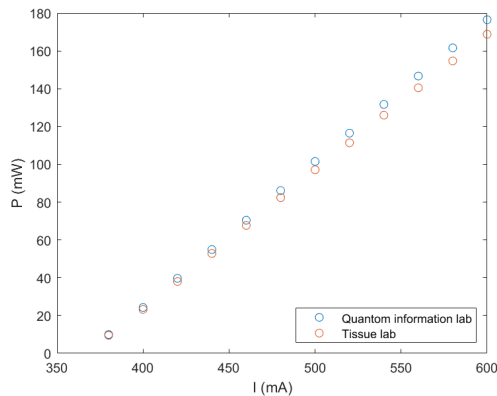
(b) Power measured through the laboratory setup for the 761 nm laser diode.



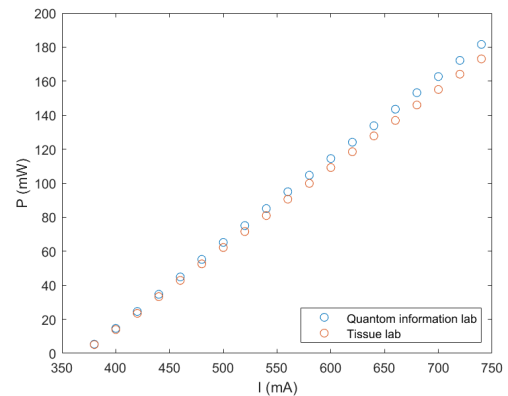
(c) Power measured close to the 937 nm laser diode surface.



(d) Power measured through the laboratory setup for the 937 nm laser diode.

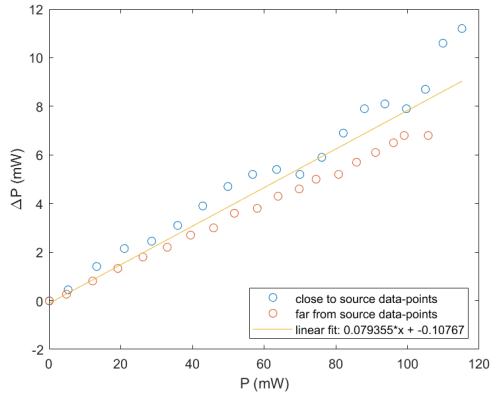


(e) Power measured close to the 971 nm laser diode surface.

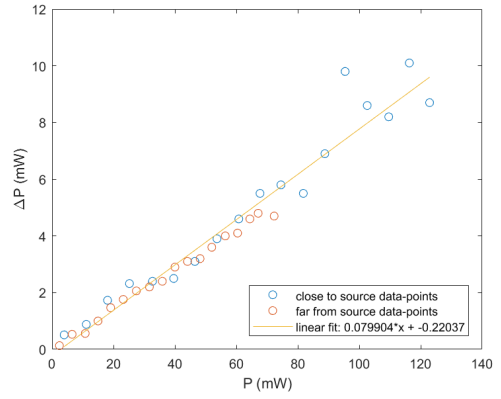


(f) Power measured through the laboratory setup for the 971 nm laser diode.

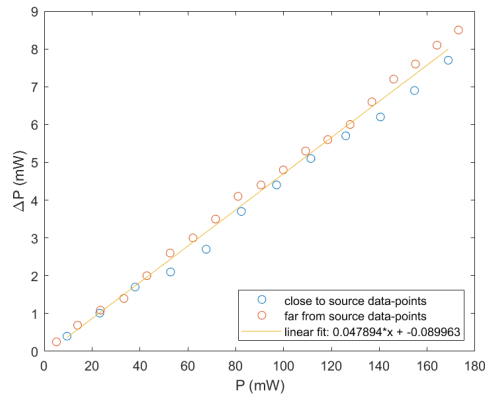
Figure 22: Measured output power through the laser drive current for by two power meters. The powers are measured very close to the laser diode and on the end of the laboratory setup for the three laser diodes.



(a) 761 nm laser diode.



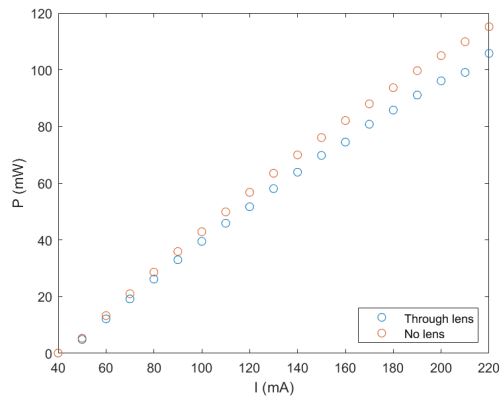
(b) 937 nm laser diode.



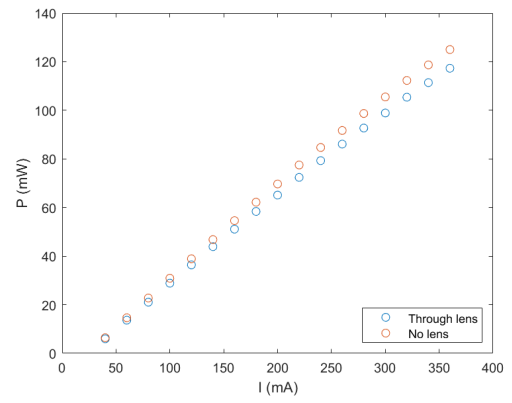
(c) 971 nm laser diode.

Figure 23: Difference between the calibrated power meter output and the uncalibrated output as a function of the uncalibrated output for each of the three laser diodes.

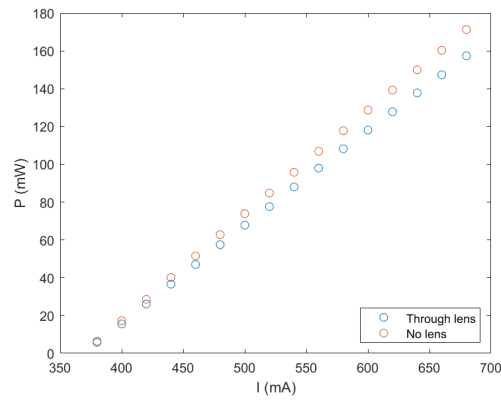
The losses in the collector lens had to be accounted for when adjusting the power levels of the lasers. As in the calibration curves the power over the measured output powers were plotted over the laser diode drive current for the three lasers, both before and after the collector lens in Figure 24. The differences were plotted in Figure 25 and a calibrational curve was extracted.



(a) 761 nm laser.

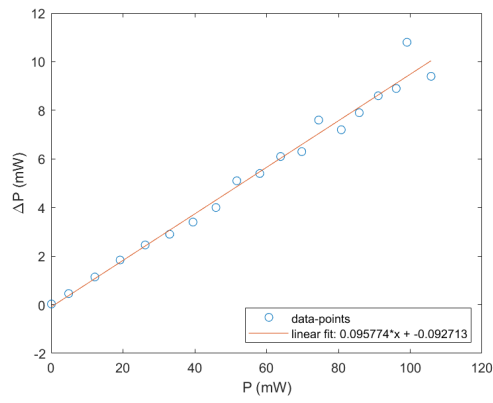


(b) 937 nm laser.

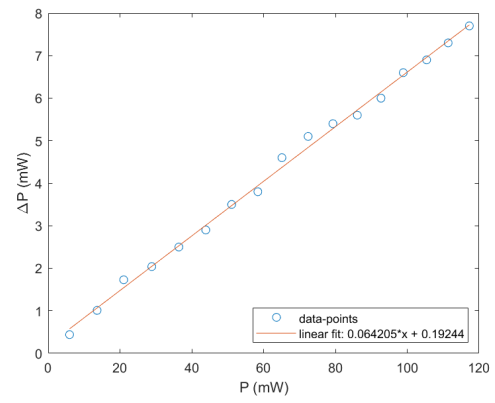


(c) 971 nm laser.

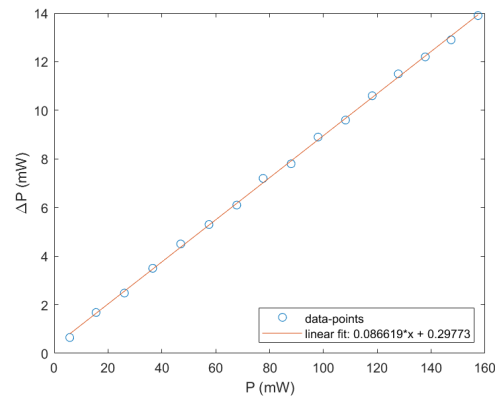
Figure 24: Measured output power through the input current for the lasers both with the beams sent through the collector lens and without the collector lens.



(a) 761 nm laser.



(b) 937 nm laser.



(c) 971 nm laser.

Figure 25: The difference between the undisturbed laser beam and the beam that was sent through the collector lens. The data was collected with the uncalibrated power meter from the tissue lab.

8.2 Appendix B - Measurement protocol

Measurement protocol – NIR tissue heating

1. Start the PC. Make sure that the heat camera (FLIR C2), IR thermometer (Optris CT-SF-C1) and camera (Thorlabs) are connected and start their respective software programs. Create a folder for today's measurement data.
2. Connect the TAC and LD cables to the desired diode house for the laser diode. Check the "act" TAC value at room temperature and set the "set" value to the same. Start TAC.
3. Start the power meter. Make sure that the right wavelength for the laser is selected and that the filter is set to "in".
4. Start the laser and place out the right optics for the desired spot-size. Make sure that the beam is aligned with the rail, is guided over the tape marking and that the height of the spot is similar to the diode height. Also make sure that the whole spot is guided from the collector lens into the power meter detector window.
5. Make sure that the highest required power can be reached in the power meter. If not, adjust the optics.
6. Place the black plastic box at the tape line and start illuminating it with the laser. Check the heat camera and IR thermometer program. Make sure that the **whole** image is visible in the heat camera and carefully adjust the IR thermometer in order to measure the highest possible temperature at a distance of 1 cm from the lens edge without interrupting the beam.
7. Shut off the laser and place the ruler at the sample tape line. Take an image with the spot-size camera where a line of at least 2cm is visible. Name the image "Spotsize_ruler_'date'.jpg" (unless moving the camera one of these rulers per day is enough).
8. Place the white paper at the sample tape line. Start the laser and make sure that the spot is visible from the camera. Set gamma to 1 and gain to 0.
9. Turn off the room light and make sure the laser is the only light source. Adjust the power so that the image is not overexposed and take an image of the spot, through the paper. Name the image "XXXnm_'Size'spot_'date'.jpg".
10. Turn on the room lights and remove the white paper from the sample stage. Adjust the power of the beam so that it matches the required power for this experiment.
11. Turn off the laser. Tape a coin onto the subject's right forearm, fully visible and normal to the heat camera lens. Place the arm on the sample stage. Make sure that some part of the arm is at the same place as the black plastic box was so that the IR thermometer measures the right spot.
12. Make sure that the IR thermometer is set to "emissivity = 0.996", and "ambient temperature = 21 degC".
13. Make sure the heat camera is set to "emissivity = 0.996", "ambient temperature = 21 degC", "output optics temperature = 21 degC" and "distance = 0.1".
14. At $t = 0$ s, start the IR thermometer from its software. At $t = 10$ s start the heat camera recording from its software. At $t = 30$ s start the laser – stay completely still. At $t = 3$ min 30 s (210 s) turn off the laser. At $t = 6$ min 30 s (390 s) stop the heat camera recording. At $t = 6$ min 40 s (400 s) stop the IR thermometer. Now you can move the arm! Save the heat camera data, without parameters in the folder as "XXXnm_XXXmW_'Size'spot_'date'.csv". Save the IR thermometer data in the folder as "XXXnm_XXXmW_'Size'spot_'date'.dat".
15. Repeat the necessary steps depending on what the next measurement is.

Power:	80 mW	100 mW	120 mW
761 nm	(67.6 mW)	(84.6 mW)	(101.5 mW)
Small spot			
Medium spot			
Large spot			
937 nm	(69.6 mW)	(87.0 mW)	(104.4 mW)
Small spot			
Medium spot			
Large spot			
971 nm	(70.2 mW)	(87.8 mW)	(105.3 mW)
Small spot			
Medium spot			
Large spot			

The power meter is uncalibrated so the calibration factor must be added for acquiring the true power (calibration). There are also losses in the collector lens that must be added (collector losses).

Wavelength (nm)	Calibration factor	Collector losses factor	Total correction factor
761	1.079	1.096	1.183
937	1.080	1.064	1.149
971	1.048	1.087	1.139